A non-canonical MPK3-ACTPK1-RbcS signalling module fine-tunes photosynthesis in rice

Sarvesh Jonwal, Gopal Banerjee, Rengasamy Balakrishnan, Mohit Mohit, Pallavi Sharma and Alok Krishna Sinha*

National Institute of Plant Genome Research, New Delhi, 110067

*Corresponding author: Alok Krishna Sinha, Email: alok@nipgr.ac.in

Short title: MPK3-ACTPK1-RbcS module fine-tunes photosynthesis

The author(s) responsible for distribution of materials integral to the findings presented in this article in accordance with the policy described in the Instructions for Authors (https://academic.oup.com/plcell/pages/General-Instructions) is: Alok Krishna Sinha (alok@nipgr.ac.in).

Abstract

Mitogen-activated protein kinase (MAPK) cascades orchestrate diverse physiological processes, yet their role in photosynthetic regulation has remained largely unexplored. Here, we uncovers a non-canonical MAPK signalling module, MITOGEN ACTIVATED PROTEIN KINASE 3 – ACT DOMAIN CONTAINING PROTEIN KINASE 1 – RUBISCO SMALL SUBUNIT (MPK3-ACTPK1-RbcS), that directly links MAPK signalling to photosynthesis optimization. ACTPK1, a dual-specificity cytosolic kinase from Group C of Raf-like MAPKKKs, is inhibited by MPK3 through direct phosphorylation. We demonstrated that ACTPK1 targets the RbcS, phosphorylating it at Thr12 within its signal peptide, thereby stabilizing its preprotein and enhancing its chloroplast import efficiency. Genetic analysis confirms that MPK3-ACTPK1-RbcS functions in a linear pathway to fine-tune photosynthesis under ambient conditions. Notably, *mpk3* knockouts boost carbon fixation by 18-21%. This non-canonical MAPK module redefines cytoplasmic-chloroplast signalling integration, offering a transformative framework for enhancing crop productivity and global food security through targeted genetic interventions.

Keywords: Photosynthesis; phosphorylation; MPK3; ACTPK1; RbcS; Rice

Introduction

Photosynthesis is the key photochemical process that drive the conversion of CO_2 and H_2O into organic carbon compounds. This process is regulated by multiple leaf traits, encompassing physiology (gas exchange, water relations, light capture), biochemistry (enzymes and metabolic pathways driving CO_2 fixation), and development (leaf structure, anatomy, and growth stage) along with external environmental factors. Photosynthetic proteins critical to this process are encoded by both the nuclear and chloroplast genomes. Chloroplast-encoded proteins are synthesized within the chloroplast, while nucleus-encoded chloroplastic proteins, are transcribed in the nucleus, translated in the cytosol, and translocated to the chloroplast via a targeting signal peptide that directs them through the chloroplast membranes (Bruce, 2000; Jarvis & López-Juez, 2013). Once inside the chloroplast, these proteins are processed and assembled into functional complexes. Rubisco, a pivotal enzyme in CO_2 fixation, is a hexadecameric holoenzyme comprising eight large subunits (RbcL) and eight small subunits (RbcS). The translocation of the small subunit into the chloroplast is essential for holoenzyme assembly. In the cytosol, the small subunit is synthesized as a precursor-RbcS with an N-terminal transit peptide, stabilized by chaperones like Hsp70 to maintain import competence, and targeted to the chloroplast's TOC complex (Lee et al., 2009, 2013; Jarvis & López-Juez, 2013). Upon reaching the chloroplast, the precursor-RbcS is translocated via the TIC/TOC translocon system, followed by cleavage of the transit peptide and folding in the stroma by chaperones like Cpn60/Cpn10 and assembly factors such as RAF1 (Spreitzer, 2003; Feiz et al., 2012; Hauser et al., 2015). The RbcS successful import and integration are critical for stabilizing the RbcL octamer and forming the functional holoenzyme; without this, Rubisco assembly fails, abolishing its CO_2 fixation capacity and severely limiting photosynthetic efficiency and thereby crop productivity (Andersson & Backlund, 2008).

Enhancing leaf photosynthesis is thus recognized as a promising strategy to improve crop yield (Long et al., 2006; Zhu et al., 2010; Gibson et al., 2011, Ort et al., 2015; Simkin et al., 2019). Biochemical insights into photosynthesis have identified key targets to overcome Rubisco's limitations, including reducing its oxygenase activity to minimize photorespiration, enhancing RuBP regeneration to support CO_2 fixation, incorporating C4 traits into C3 plants, and suppressing photorespiration (Long et al., 2006; Zhu et al., 2010; Murchie & Niyogi, 2011; Gibson et al., 2011; Ort et al., 2015; Simkin et al., 2019). These targets address the primary biochemical constraints on leaf photosynthesis: the *in vivo* Rubisco activity (*Vcmax*), the

electron transport rate (*J*) that controls RuBP regeneration, and the rate of triose phosphate utilization (*TPU*) (Farquhar et al., 1980; Sharkey, 1985; von Caemmerer, 2000). These parameters are typically derived from the response of net CO_2 assimilation to intercellular CO_2 concentration under saturating light (*A/Ci* curve) (Long & Bernacchi, 2003; Sharkey et al., 2007).

At low intercellular CO_2 levels (<200 µmol mol^{-1}), Rubisco's low catalytic efficiency and competing oxygenase activity dominate photosynthetic limitations, reducing carbon assimilation by promoting photorespiration (von Caemmerer, 2000; Parry et al., 2007; Sharkey et al., 2007). Potential Strategies to mitigate this constraint include engineering Rubisco with improved specificity for CO_2 over O_2, enhancing CO_2 delivery to its active site via increased stomatal and mesophyll conductance, or introducing CO_2-concentrating mechanisms like C4 traits to reduce photorespiratory losses (Parry et al., 2007, 2013; Lin et al., 2014; Sharwood, 2017). At higher CO_2 concentrations (>300 µmol mol^{-1}), limitations shift to electron transport and RuBP regeneration, influenced by photosystem efficiency and light-harvesting organization (Murchie & Lawson, 2013; Wu et al., 2019), and to TPU, where saturation of triose phosphate conversion into sucrose and starch causes feedback inhibition, capping maximum photosynthetic capacity (*Amax*) (Sharkey et al., 2007; Fabre et al., 2019). Developmental traits, such as leaf anatomy and light distribution, further modulate Rubisco's effectiveness by optimizing light capture and CO_2 diffusion (Terashima et al., 2011; Mathan et al., 2016). Targeting these interconnected factors offers promising avenues for enhancing Rubisco-driven photosynthetic efficiency and crop productivity (Evans, 2013).

Photosynthetic efficiency is further modulated by environmental fluctuations, such as light, temperature, and CO_2 concentration, which impact Rubisco activity, electron flow, and carbon assimilation (Kalaji et al., 2016; Sharma et al., 2020; Gao et al., 2024). To maintain optimal photosynthesis under these conditions, plants employ post-translational modifications along with gene expression at transcriptional and translational levels, with phosphorylation playing a central role (Puthiyaveetil et al., 2009, 2010; Schönberg & Baginsky, 2012; Jonwal et al., 2021; Xiong D, 2024). Phosphorylation, mediated by kinases such as STN7, STN8, and cpCK2α, targets core photosystem proteins, light harvesting complexes, plastid transcription factors and Calvin cycle enzymes. They function by modulating their activity, stability, and interactions to balance electron flow, protect against photoinhibition, and optimize CO_2 fixation (Bellafiore et al., 2005; Reiland et al., 2009, 2011; Schönberg et al., 2017). While phosphorylation is a well-established mechanism in photosynthetic regulation, the role of Mitogen-Activated Protein Kinase (MAPK) cascades in this context remains underexplored.

MAPK cascades are conserved signalling pathways in eukaryotes. They operate in three tiers: MAPKKKs activate MAPKKs at a conserved S/T-X5-S/T motif, which in turn activate MAPKs at the TE/DY motif (Hamel et al., 2006). This hierarchical cascade ensures precise signal transmission, with MAPKKKs as initiators, MAPKKs as intermediates, and MAPKs as terminal effectors that phosphorylate substrates to regulate cellular responses (Rodriguez et al., 2010). MAPKs regulates growth, development, immunity, and defence in response to environmental and endogenous cues (Sinha et al., 2011; Manna et al., 2023). Evidence from multiple plant systems highlights MAPKs as important regulators of photosynthesis. In *Nicotiana attenuata* and *Arabidopsis*, MPK4 influences stomatal conductance, thylakoid organization, and PSII efficiency, thereby affecting carbon assimilation and energy distribution (Hettenhausen et al., 2012; Gawronski et al., 2014; Witoń et al., 2016, 2021). Moreover, *StMPK3*, *StMPK11*, and *PeMPK7*, modulate photosynthetic gene expression and stomatal dynamics under stress (Zhu et al., 2020, 2021; Gao et al., 2024). Furthermore, MPK4, MPK12, regulate CO_2-induced stomatal behaviour through Raf-like MAPKKK *HT1* (Hashimoto et al., 2016; Hiyama et al., 2017; K. Tõldsepp et al., 2018; Takahashi et al., 2022). MPK3 and MPK6

are rapidly activated during stress and immunity and often correlate with reduced photosynthetic activity (Su et al., 2018). Consistent with this, MPK3 overexpression has been shown to strongly reduce photosynthetic performance, whereas MPK6 exerts a modest positive effect, highlighting their distinct roles even under non-stressful conditions (Jonwal et al., 2023). However, the precise molecular mechanisms by which MAPKs influence photosynthesis remain poorly understood.

Here, we identify a previously unknown signalling cascade linking MPK3 to photosynthetic regulation. MPK3 suppresses photosynthesis by phosphorylating and inhibiting the Raf-like MAPKKK, ACTPK1, which in turn stabilizes and facilitates the import of RbcS into chloroplast. ACTPK1 is a cytosolic serine/threonine kinase first identified in rice as an interactor and regulator of ammonium transporters. It phosphorylates AMT1 transporters to modulate ammonium uptake, thereby linking nutrient signalling to cellular homeostasis (Beier et al., 2018). Structural analyses indicate that ACTPK1 belongs to the STY kinase family (Rudrabhatla et al., 2006). Sequence similarity and phylogenetic analyses place ACTPK1 within the Group C Raf-like MAPKKKs (Rao et al., 2010). Homologues of ACTPK1 in Arabidopsis (STY8, STY17 & STY46) are implicated in chloroplast biogenesis, chlorophyll biosynthesis, pre-protein trafficking into chloroplast and photosynthetic performance at PSII (Lamberti et al., 2011). Our findings, the MPK3–ACTPK1–RbcS module reveals a non-canonical MAPK pathway that fine-tunes photosynthetic efficiency in rice.

Results

MPK3 negatively regulates photosynthetic Carbon Assimilation

Overexpression of *MPK3* has been reported to adversely affects photosynthetic performance in rice (Jonwal et al., 2023). To dissect the molecular mechanism underlying this observation, we analysed the photosynthesis and related parameters in two independent *MPK3* knockout lines (*mpk3 ko1* and *mpk3 ko2*) and two dexamethasone (DEX)-inducible *MPK3* overexpression lines (*MPK3-23* and *MPK3-24*) under ambient growth conditions (Banerjee et al., 2025; Singh et al., 2019). This approach allowed us to investigate both loss- and gain-of-function effects of MPK3, providing insights into its regulatory role.

Quantitative measurements of photosynthetic pigments revealed that *mpk3 ko* plants accumulated significantly higher levels of chlorophyll a, chlorophyll b, and carotenoids compared to WT, whereas these pigments were markedly reduced in *MPK3 OE* lines (Supplemental Fig. S1A-D). These pigments are essential for light absorption and photoprotection in photosynthesis; thus, elevated levels in knockout lines likely enhance light-harvesting efficiency and overall photosynthetic capacity, while reduced levels in overexpression lines may impair these processes. Consistent with this, the mean net CO_2 assimilation rate (*A*) in *mpk3 ko* lines were significantly higher than WT whereas it was significantly lower in *MPK3 OE* lines (Fig. 1A). Under ambient CO_2 concentration (400 µmol CO_2 mol^{-1}), the mean *A* was 29.78 µmol CO_2 m^{-2} s^{-1} and 30.48 µmol CO_2 m^{-2} s^{-1} for *mpk3 ko1 and mpk3 ko2* respectively, representing an 18-21% increase over WT. In contrast, *MPK3 OE* lines showed mean *A* at 17.75 µmol CO_2 m^{-2} s^{-1} and 17.67 µmol CO_2 m^{-2} s^{-1} which is ~29% lower than WT (Table 1).

Photosynthetic efficiency depends on CO_2 diffusion into the chloroplast stroma (stomatal conductance, *gs*) and its subsequent fixation (carboxylation efficiency). CO_2 diffusion is constrained by barriers encountered along the path from stomata to the chloroplast envelope (Evans, 2021). To explore the basis for the observed differences in *A*, we measured *gs* and intercellular CO_2 concentration (*Ci*). Notably, *mpk3 ko* plants with higher *A* exhibited elevated

159 *gs* whereas *MPK3 OE* plants showed reduced *gs* compared to WT. However, C_i values
160 remained comparable across genotypes (Fig. 1B and Supplemental Fig. S1E), indicating that
161 the altered photosynthetic rates stem primarily from differences in carboxylation efficiency
162 rather than CO_2 availability.

163 Given that *mpk3 ko* showed higher stomatal conductance and assimilation rates, yet similar
164 intercellular CO_2 levels, suggesting differences in carboxylation efficiency, we used *A/Ci* and
165 *A/Q* curves to determine whether MPK3 regulates CO_2 fixation or light-dependent processes
166 (Farquhar et al., 1980; Long & Bernacchi, 2003). With increasing CO_2, *mpk3 ko* plants
167 exhibited consistently higher *A* compared to WT, with a CO_2-saturated maximum assimilation
168 rate (*Amax*) of 41.31 ± 0.68 µmol CO_2 m^{-2} s^{-1} (~14% higher than WT), while *MPK3 OE* lines
169 showed a reduced *Amax* of 27.55 ± 1.45 µmol CO_2 m^{-2} s^{-1} (~31% lower than WT) (Fig. 1C
170 and Table 1). However, no significant differences in *A* were observed among genotypes with
171 increasing photosynthetic photon flux density (PPFD), and light-saturated *Amax* values were
172 comparable (Fig. 1D). These findings align with the *gs* and *Ci* data, confirming that MPK3
173 regulates CO_2-responsive aspects of photosynthesis, such as Calvin cycle efficiency, rather
174 than light-dependent processes like light harvesting or electron transport.

175 To understand the biochemical factors limiting CO_2 fixation, especially carboxylation
176 efficiency, we used the Farquhar-von Caemmerer-Berry (FvCB) model to analyze *A/Ci* curve
177 data and calculate the *Vcmax*, *J*, and *TPU*. These parameters are pivotal, as *Vcmax* reflects
178 Rubisco's CO_2 fixation capacity, *J* supports energy supply for the Calvin cycle, and *TPU*
179 governs product export and RuBP regeneration, all of which limit photosynthetic yield. Our
180 results showed that *Vcmax*, *J*, and *TPU* were significantly enhanced in *mpk3 ko* plants but
181 markedly reduced in *MPK3 OE* lines compared to WT (Fig. 1E, F & G). These results establish
182 *MPK3* as a negative regulator of photosynthetic efficiency, as knockout lines exhibited
183 enhanced pigment accumulation, stomatal conductance, and carboxylation efficiency, boosting
184 photosynthesis, while overexpression lines showing the opposite trend.

185 **MPK3 Regulates Rubisco Activity via RbcS Phosphorylation**

186 Carboxylation efficiency is primarily governed by Rubisco, the enzyme catalysing the reaction
187 of CO_2 with RuBP to form 3-phosphoglycerate (Farquhar et al., 1980). The efficiency of
188 Rubisco depends on its catalytic activity and the availability of RuBP as a substrate. To
189 investigate how MPK3 affects Rubisco function and substrate dynamics, we conducted RuBP
190 use and Rubisco activity assays in *mpk3 ko* lines. Our results revealed significantly higher
191 Rubisco activity and RuBP use in *mpk3 ko* lines compared to WT, aligning with the enhanced
192 *Vcmax* in these lines (Fig. 1H, I). These results indicates that MPK3 acts as a negative regulator
193 of Rubisco function and RuBP regeneration, thereby limiting carboxylation efficiency and
194 photosynthetic capacity in rice plant.

195 Rubisco activity depends on the assembly of RbcL and RbcS into the holoenzyme complex.
196 Given that RbcS is encoded by nuclear genes while RbcL is transcribed from the chloroplast
197 genome, and considering MPK3's predominant localization to the nucleus and cytosol
198 (Supplemental Fig. S2A & B), we hypothesised that MPK3 regulates Rubisco function through
199 transcriptional or post-translational modulation of RbcS expression or stability, rather than
200 direct interaction with chloroplast-resident RbcL.

201 To explore whether MPK3 influences RbcS post-translationally, we investigated its potential
202 role in RbcS phosphorylation. Using Phos-tag PAGE, which separates phosphorylated proteins
203 by reducing their electrophoretic mobility, we detected an upshifted RbcS band indicative of
204 phosphorylation in both WT and *mpk3 ko* plants. Notably, the phosphorylated RbcS band was
205 consistently more intense in *mpk3 ko* plants compared to WT, suggesting enhanced RbcS

206 phosphorylation in the absence of *MPK3* (Fig. 1J). This higher RbcS phosphorylation in *mpk3*
207 *ko* is positively correlated with higher Rubisco activity and carboxylation rates.

208 These findings imply that MPK3 does not directly phosphorylate RbcS but rather suppresses
209 the activity of another kinase responsible for this modification. In *mpk3 ko* plants, where MPK3
210 is absent, this another "missing" kinase remains active, leading to increased RbcS
211 phosphorylation. Given the functional overlap between MPK3 and MPK6, we tested whether
212 MPK6 could act as this "missing" kinase. However, yeast two-hybrid (Y2H) and *in vitro* kinase
213 assays revealed no interaction or phosphorylation of RbcS by either MPK3 or MPK6
214 (Supplemental Fig. S2C & D), ruling out MPK6 as the "missing" kinase. These findings
215 suggest that MPK3 indirectly modulates Rubisco activity by regulating RbcS phosphorylation
216 via an unidentified kinase.

217 **Identification of ACTPK1 as a Candidate "missing" Kinase**

218 To identity the kinase responsible for elevated phosphorylation of RbcS in *mpk3 ko* lines, we
219 conducted a literature survey focusing on known kinases that modify RbcS or its precursor. In
220 *Arabidopsis thaliana*, the RbcS precursor is phosphorylated by three cytosolic plant-specific
221 STY kinases, STY8, STY17, and STY46, which specifically target the transit peptide to
222 facilitate regulated import into the chloroplast, thereby influencing Rubisco assembly and
223 photosynthetic efficiency (Lamberti et al., 2011). To identify the functional homolog of these
224 STY kinases in rice, we conducted a sequence homology search using *At*STY46 as a query
225 sequence in the NCBI BLAST database. This analysis identified an ACT domain containing
226 protein kinase encoded by LOC_Os02g02780 (Supplemental Fig. S3A), which was named as
227 ACTPK1 by Beier et al (2018). Sequence similarity and phylogenetic analyses place ACTPK1
228 within the Group C Raf-like MAPKKKs (Rao et al., 2010) (Supplemental Fig. S3B). ACTPK1
229 exhibit significant similarities in its protein sequence with STY8, STY17 and STY46
230 respectively (Supplemental Fig. S3C). Importantly, the ACTPK1 protein sequence contains
231 multiple canonical S/TP motifs, representing consensus phosphorylation sites of MPK3
232 (Supplemental Fig. S3D), suggestive of potential regulatory crosstalk between MPK3 and
233 ACTPK1. Given these structural and sequence similarities, ACTPK1 emerges as a strong
234 candidate for the kinase suppressed by MPK3 in regulating RbcS phosphorylation.

235 **MPK3 physically interacts with ACTPK1**

236 To confirm whether ACTPK1 is the kinase modulated by MPK3 in our hypothesis, we aim to
237 investigate its regulation by MPK3. Since MPK3 typically regulate downstream targets through
238 direct interaction followed by phosphorylation (Manna et al., 2023), we first examined whether
239 ACTPK1 physically associates with MPK3. For doing this, we employed various protein–
240 protein interaction assays.

241 We initially assessed the interaction between ACTPK1 and MPK3 in yeast cell
242 (*Saccharomyces cerevisiae*) using Y2H assay. ACTPK1 fused to the GAL4 DNA-binding
243 domain (BD) and MPK3 fused to the GAL4 activation domain (AD), were co-transformed into
244 the Y2H Gold strain in different combinations. Transformants were screened on double dropout
245 (DDO; SD/-Trp/-Leu) and quadruple dropout (QDO; SD/-Trp/-Leu/-His/-Ade**)** medium to
246 assess protein interaction. Experimental results showed that MPK3 interacts with ACTPK1 in
247 yeast cell (Fig. 2A). The well-established p53–T7 pair (pGADT7-T7 + pGBKT7-p53) was used
248 as a positive control, while the empty vector combinations **(**pGADT7 + pGBKT7**)** served as
249 negative controls.

250 To validate this interaction *in planta*, we carried out bimolecular fluorescence
251 complementation (BiFC) assays in *Nicotiana benthamiana* leaves. ACTPK1 was fused to the
252 N-terminal half of enhanced yellow fluorescent protein (nYFP), while MPK3 was fused to the

253 C-terminal half (cYFP). The constructs were transiently co-expressed in fully expanded leaves
254 of *N. benthamiana.* Strong YFP fluorescence was observed in cells co-expressing ACTPK1-
255 nYFP and MPK3-cYFP (Fig. 2B). No fluorescence signal was detected in control combinations
256 (ACTPK1-nYFP + cYFP-empty, MPK3-cYFP + nYFP-empty and ACTPK1-nYFP + MPK6-
257 cYFP), further confirming the specificity of the interaction in plant cells.

258 The physical association between ACTPK1 and MPK3 was further confirmed by co-
259 immunoprecipitation (Co-IP) assays. Flag-tagged ACTPK1 and GFP-tagged MPK3 were
260 transiently co-expressed in *N. benthamiana* leaves, and total proteins were extracted 48 h post-
261 infiltration. Immunoprecipitation with anti-Flag antibody followed by immunoblotting with
262 anti-GFP antibody revealed the presence of MPK3-GFP in the ACTPK1-Flag
263 immunocomplex, demonstrating that ACTPK1 associates with MPK3 *in vivo* (Fig. 2C). No
264 signal was detected in control sample where ACTPK1-Flag and empty-GFP were co-
265 expressed, thus excluding the possibility of nonspecific binding.

266 Collectively, these results provide conclusive evidence that MPK3 physically interacts with
267 ACTPK1. Building on this established physical association, we next examined whether MPK3
268 functionally regulates ACTPK1 via phosphorylation.

269 **MPK3 phosphorylates ACTPK1 and supress its kinase activity**

270 As a putative Raf like MAPKKK, ACTPK1 was predicted to exhibit kinase activity. To test
271 this possibility, the coding sequence of ACTPK1 was fused with glutathione S-transferase
272 (GST) for protein purification. The resultant purified protein was subjected to *in vitro* kinase
273 assay with myelin basic protein (MBP), a widely used universal kinase substrate (Eichberg and
274 Iyer, 1996). Briefly, GST-ACTPK1 was incubated with MBP in kinase assay buffer
275 supplemented with λ^{32}P-ATP for 30 min at 30°C and and the reaction products were resolved
276 by SDS-PAGE. Autoradiography revealed strong phosphorylation signals corresponding to
277 both ACTPK1 and MBP, indicating that ACTPK1 possesses both auto- and trans-
278 phosphorylation activities (Supplemental Fig. S4A).

279 To test whether ACTPK1 could serve as a substrate of MPK3, we first generated a kinase-dead
280 variant of ACTPK1 that would not produce background phosphorylation signals. Kinase
281 activity is attributed by the catalytic domain of a protein kinase. Sequence of catalytic domain
282 among protein kinases showed a remarkable degree of similarity and are conserved from yeast
283 to humans (Hanks et al., 1988). The conserved lysine residue present in the subdomain II of
284 catalytic domain is involved in the phosphor-transfer reactions (Carrera et al., 1993).
285 Substitution of this invariant lysine with another amino acid, such as arginine, typically
286 abolishes kinase activity (Snyder et al., 1985; Kamps and Sefton, 1986). To make catalytically
287 inactive variant of ACTPK1, we align the protein sequence of ACTPK1 with its homologues
288 using clustal O (1.2.4) and identified a conserved lysine (at 332 position) in the predicted
289 catalytic active site (subdomain II) (Supplemental Fig. S4B). We mutated this conserved lysine
290 to arginine (ACTPK1^{K332R}) using site directed mutagenesis (Supplemental Fig. S4C) and fused
291 it with GST for protein expression and purification. To test whether the mutation of lysine to
292 arginine rendered ACTPK1 kinase dead or not, we performed an *in vitro* kinase assay using
293 λ^{32}P-ATP, with MBP as substrate. Experimental results showed that MBP phosphorylation was
294 abolished, however, auto-phosphorylation was still present (Supplemental Fig. S4A). This
295 result suggests that lysine residue at 332 position is essential for trans-phosphorylation activity
296 of ACTPK1, but not for autophosphorylation.

297 To deduce the site responsible for auto-phosphorylation activity, we again scanned the
298 ACTPK1 sequence and identified a second conserved lysine at position 428, located within the
299 predicted catalytic active site (subdomain VI) (Supplemental Fig. S4B). Using site directed

300 mutagenesis, we mutated this lysine into arginine (K428R) in the background of ACTPK1^{K332R}
301 (denoted as ACTPK1^{K332R,K428R}) (Supplemental Fig. S4D). To assess ACTPK1^{K332R,K428R} for
302 auto-phosphorylation activity, an *in vitro* kinase assay was conducted with MBP as a substrate.
303 *In vitro* kinase assays revealed a complete loss of both auto- and trans-phosphorylation activity
304 in ACTPK1^{K332R,K428R} (Supplemental Fig. S4A). Overall, the results demonstrate that lysine at
305 332 is required for trans-phosphorylation, while lysine at 428 is indispensable for auto-
306 phosphorylation activity of ACTPK1.

307 To determine the phosphorylation of ACTPK1 by MPK3, an in-solution kinase assay was
308 performed using kinase dead variant (ACTPK1^{K332R,K428R}) as substrate. The assay was
309 conducted at 30°C for 30 minutes, following which the reaction mixture was resolved on a 10%
310 SDS-PAA gel.

311 The results showed that MPK3 phosphorylates ACTPK1^{K332R,K428R}, as indicated by the
312 presence of a signal on the autoradiogram corresponding to the molecular weight of ACTPK1
313 (Fig. 2D). GST protein was included in the assay as a negative control and as expected, no
314 signal corresponding to the size of GST was observed on the autoradiogram, confirming the
315 specificity of MPK3-mediated phosphorylation of ACTPK1^{K332R,K428R}. These findings provide
316 strong evidence that MPK3 directly phosphorylates ACTPK1, suggesting a potential regulatory
317 interaction between these proteins.

318 In *Medicago sativa*, OMTK1 (a MAPKKK) was shown to directly phosphorylate and activate
319 the MMK3 (a MAPK), bypassing the canonical MAPKK step (Nakagami et al., 2004). This
320 represents a rare exception to the typical three-tier MAPK cascade and highlights alternative
321 signalling modes in plants. Given that ACTPK1 being a MAPKK kinase member, the
322 possibility of reverse phosphorylation, wherein ACTPK1 phosphorylates MPK3, was also
323 investigated. To assess this, an *in vitro* phosphorylation assay was performed using a kinase-
324 dead variant of MPK3 (MPK3^{K65R}) as the substrate, with ACTPK1 serving as the kinase. The
325 results indicated that ACTPK1 does not phosphorylate MPK3, as no detectable signal
326 corresponding to the molecular weight of MPK3^{K65R} was observed on the autoradiogram
327 (Supplemental Fig. S4E). This finding suggests that phosphorylation occurs in a unidirectional
328 manner, wherein MPK3 phosphorylates ACTPK1, but not vice versa.

329 We then explored the functional relevance of MPK3-driven phosphorylation of ACTPK1. To
330 investigate this, we performed an immunoprecipitation-kinase (IP-kinase) assay using protein
331 extracts from WT and *mpk3 ko* plants and MBP as substrate. ACTPK1 was immunoprecipitated
332 from total protein extracts of WT and *mpk3 ko* plants using an α-ACTPK1 antibody, and the
333 immunoprecipitated fraction was subjected to *in-solution* kinase assays with MBP as substrate.
334 Interestingly, MBP phosphorylation was substantially stronger in immunoprecipitants from
335 *mpk3 ko1* and *mpk3 ko2* lines, whereas only a faint phosphorylation signal was observed in
336 WT samples (Fig. 2E). These results indicate that MPK3 negatively regulates the kinase
337 activity of ACTPK1, likely through direct phosphorylation-mediated inhibition.

338 **ACTPK1 interacts with and phosphorylates RbcS at its signal peptide**

339 To establish ACTPK1 as a kinase of our hypothesis, it must phosphorylate RbcS. In rice, RbcS
340 is encoded by five isoforms, among which RbcS3 accounts for ~50% of the total pool and was
341 therefore selected for further analysis (Suzuki et al., 2007). Because ACTPK1 is a cytosolic
342 kinase, we reasoned that any potential interaction with RbcS would most likely occur in the
343 cytoplasm prior to plastid import. To capture this event, we used the pre-sequence form of
344 RbcS in our interaction assays.

345 To test the physical association between ACTPK1 and RbcS, we first performed Y2H assays,
346 where ACTPK1 was fused to the GAL4 activation domain and RbcS to the GAL4 DNA-

binding domain. Yeast co-transformants grew robustly on both double dropout (DDO) and quadruple dropout (QDO) selective media, indicating a direct interaction between ACTPK1 and RbcS (Fig. 3A).

To validate this interaction *in planta*, we conducted BiFC assays. ACTPK1 was fused to the N-terminal half of YFP (nYFP) and RbcS to the C-terminal half (cYFP), and the constructs were co-expressed in *N. benthamiana* leaves by *Agrobacterium* infiltration. Strong YFP fluorescence was observed 48 h post-infiltration in the cytoplasm, confirming that ACTPK1 physically interacts with RbcS *in vivo* (Fig. 3B). Together, these results demonstrate that ACTPK1 physically associates with RbcS in the cytoplasm, suggesting a regulatory role in Rubisco assembly or function.

We next investigated whether the physical interaction between ACTPK1 and RbcS results in phosphorylation of RbcS. To address this, we performed *in vitro* kinase assays using bacterially expressed and purified GST-ACTPK1 and GST-RbcS. A strong phosphorylation signal was detected on RbcS, confirming that ACTPK1 directly phosphorylates RbcS (Fig. 3C).

To pinpoint the region of phosphorylation, we cloned and expressed precursor RbcS (containing the signal peptide) and its mature form lacking the signal peptide (mRbcS). Kinase assays revealed that phosphorylation occurred exclusively on the precursor RbcS but was abolished in mRbcS, indicating that the phosphorylation site resides within the signal peptide region (Supplemental Fig. S5A & B).

In silico prediction using NetPhos3.1 identified three high-confidence candidate phosphorylation sites within the signal peptide—Thr12, Ser31, and Ser34 (Supplemental Fig. S5C). To experimentally validate these sites, we generated alanine substitution mutants ($RbcS^{S31A}$, $RbcS^{S34A}$ and $RbcS^{T12A}$) and tested them in kinase assays (Supplemental Fig. S5D). Phosphorylation was retained in $RbcS^{S31A}$ and $RbcS^{S34A}$ but was completely abolished in $RbcS^{T12A}$, demonstrating that Thr12 is the specific residue phosphorylated by ACTPK1 (Fig. 3D, Supplemental Fig. S5E).

Together, these findings demonstrate that ACTPK1 directly phosphorylates RbcS at Thr12 within its signal peptide. This modification likely act as a regulatory checkpoint in the cytoplasm, modulating RbcS import into chloroplasts and thereby fine-tuning Rubisco assembly and function.

Phosphorylation by ACTPK1 is essential for chloroplast targeting of RbcS

Since ACTPK1 phosphorylates RbcS within its signal peptide, we hypothesized that this modification may influence RbcS translocation into chloroplasts. To test this, we generated phospho-mimic and phospho-dead variants of precursor RbcS by site-directed mutagenesis using overlapping PCR. Specifically, threonine at position 12, the residue phosphorylated by ACTPK1, was mutated to glutamic acid ($RbcS^{T12D}$) to mimic constitutive phosphorylation, and to alanine ($RbcS^{T12A}$) to prevent phosphorylation (Fig. 4A). GFP was fused to wild-type precursor RbcS ($RbcS^{WT}$), phospho-mimic ($RbcS^{T12D}$), and phospho-dead ($RbcS^{T12A}$) at C-terminal region and transiently expressed in rice protoplasts derived from WT, *mpk3 ko*, and *actpk1 ko* backgrounds.

In WT protoplasts, RbcS localized exclusively to chloroplasts, whereas $RbcS^{T12D}$ accumulated as aggregates adjacent to chloroplasts but failed to enter the chloroplast (Fig. 4B), consistent with the requirement for dephosphorylation of transit peptides prior to TOC/TIC translocation (Waegemann & Soll, 1996; Jarvis and Robinson, 2004). In contrast, $RbcS^{T12A}$ displayed dual localization between chloroplasts and the cytoplasm (Fig. 4B), indicating that while phosphorylation at Thr12 optimizes precursor recognition and import, a phosphorylation-

independent Hsp90/Hsp70-dependent route can partially compensate (May & Soll, 2000). In *mpk3 ko* protoplasts, RbcS was exclusively localised to the chloroplast (Fig. 4C).

Strikingly, in *actpk1 ko* protoplasts, no GFP signal was detected for any RbcS variant despite multiple independent attempts (Supplemental Fig. S6). This puzzled us, so we hypothesised, what if, in the absence of ACTPK1, RbcS isn't just not imported but degraded? To test this, we performed cell-free degradation assays using bacterially expressed RbcS protein. RbcS was rapidly degraded in the crude extract from *actpk1 ko* seedlings but remained stable in WT and *mpk3 ko* crude extracts (Fig. 4D), demonstrating that ACTPK1-mediated phosphorylation stabilizes RbcS in the cytoplasm prior to import. This is consistent with prior reports that import-defective precursors are recognized by Hsc70-4/CHIP complexes and targeted for proteasomal degradation (Lee et al., 2009; Jarvis & López-Juez, 2013). Together, these findings suggest that ACTPK1-mediated phosphorylation ensures early handling of RbcS precursors simultaneously protecting them from premature cytosolic degradation.

ACTPK1 positively regulates photosynthesis

To further validate this pathway and its impact on photosynthesis, we generated *ACTPK1* overexpression (*OE*) and knockout (*ko*) lines, along with *MPK3-ACTPK1* double knockout (*mpk3actpk1 ko*) in the japonica rice cultivar Taipae309. Three independent *OE* lines (*ACTPK1 OE19*, *ACTPK1 OE24* and *ACTPK1 OE33*) with the highest transcript accumulation were selected for detailed analysis (Supplemental Fig. S7A, B & C). *actpk1 ko* lines were generated via CRISPR/Cas9-mediated genome editing technology and three independent *actpk1* mutant alleles, *actpk1 ko12* (deletion of four nucleotides), *actpk1 ko14* (single nucleotide insertion) and *actpk1 ko19* (single nucleotide insertion), were selected for detailed analysis (Supplemental Fig. S7D & E). The double knockout was generated by mutating ACTPK1 in *mpk3 ko* background using CRISPR-Cas9 genome editing tool. A mutant line harbouring a single-nucleotide insertion in the ACTPK1 coding sequence was selected for further analysis (Supplemental Fig. S7F).

To study the impact of ACTPK1 on photosynthesis we measured gas-exchange parameters in the flag leaf of *ACTPK1 OE* and *actpk1 ko* lines at heading stage using LI-COR 6800 system, targeting a 2 cm^2 area from 9:00 am to 11:00 am. At ambient CO_2 concentration, the mean *A* of *actpk1 ko* plants were significantly lower that WT and *ACTPK1 OE* lines, with *actpk1 ko* showing 12.973 ± 0.99 μmol m^{-2} s^{-1}, a 36–45% decrease compared to WT and *ACTPK1 OE* plants (Fig. 5A & Table 2). In contrast, mean *A* in *ACTPK1 OE* lines were comparable to WT, indicating that overexpression does not disturb the kinase's functional balance.

Photosynthesis is positively corelated with stomatal conductance. Stomatal conductance mirrored these patterns, with *actpk1 ko* lines showing lower values consistent with reduced photosynthetic capacity (Fig. 5B). *Ci* remained unchanged among genotypes, ruling out CO_2 availability as the cause of reduced photosynthesis in *actpk1 ko* plants. (Supplemental Fig. 8).

Moreover, *A/Ci* response curves revealed a pronounced reduction in net photosynthetic rate in *actpk1 ko* lines compared to WT and *ACTPK1 OE* lines across all tested CO_2 concentrations (Fig. 5C). Interestingly, *ACTPK1 OE* lines exhibited photosynthetic rates comparable to WT across all tested CO_2 concentrations. *A/Q* curves further showed that *actpk1 ko* lines had diminished light-saturated photosynthesis, while *ACTPK1 OE* lines sustained slightly higher rates relative to WT (Fig. 5D).

Modelling of the *A/Ci* curves provided further insight into the biochemical basis of this decline. The CO_2-saturated photosynthetic capacity (A_{max}) was reduced by ~31–37% in *actpk1 ko* plants (26.2 ± 0.5 μmol m^{-2} s^{-1}) compared with WT (39.3 ± 0.8 μmol m^{-2} s^{-1}) and *OE* lines (39.9 ± 1.5 μmol m^{-2} s^{-1}) (Table 2). Moreover, *actpk1 ko* lines displayed significantly reduced values

440 for *Vcmax*, *J*, and *TPU* (Fig. 5E, F & G). These reductions strongly suggest impaired Rubisco
441 activity and compromised electron transport in *actpk1 ko* plants. Collectively, these findings
442 demonstrate that the absence of ACTPK1 leads to a substantial loss in Rubisco-dependent
443 photosynthetic capacity.

444 **MPK3-ACTPK1 operate in a linear signalling cascade to regulate photosynthesis**

445 Next, we analysed the photosynthetic phenotypes of *mpk3*, *actpk1*, and *mpk3actpk1* mutants.
446 *A/Ci* response curves revealed a marked increase in net CO_2 assimilation in *mpk3 ko* plants,
447 with a steep rise and elevated plateau, whereas *actpk1 ko* lines displayed strongly reduced
448 photosynthetic rates relative to WT, across a range of intercellular CO_2 concentrations (Fig.
449 6A). Crucially, the *mpk3actpk1* double mutant mirrors the *actpk1 ko* phenotype, with low
450 assimilation rate, rather than the enhanced *mpk3 ko* mutant. This suppression in the
451 *mpk3actpk1* double mutant indicates that ACTPK1 is required for the photosynthetic benefits
452 of MPK3 absence; without ACTPK1, knocking out MPK3 cannot rescue the pathway. A
453 similar trend was observed for light response (*A/Q*) curves where *mpk3 ko* plants maintained
454 slightly elevated photosynthetic rates under increasing irradiance, while *actpk1 ko* and
455 *mpk3actpk1 ko* lines exhibited impaired light-saturated photosynthesis (Fig. 6B).

456 Moreover, the biochemical insights support the above observations. *Vcmax* was highest in
457 *mpk3 ko* lines but drops to *actpk1 ko* levels in and *mpk3actpk1 ko* plants. *J* and *TPU* followed
458 the same trend, enhanced in *mpk3 ko*, and reduced in *actpk1 ko* and *mpk3actpk1 ko* plants
459 compared to WT. (Fig. 6C, D & E). Rubisco activity measurements further confirmed this
460 trend, with higher activity in *mpk3 ko* and strongly diminished activity in *actpk1 ko* and
461 *mpk3actpk1 ko* (Fig. 6F, G).

462 The finding that *mpk3actpk1* double mutants phenocopy the *actpk1 ko* mutants, rather than
463 *mpk3 ko* alone, indicates that ACTPK1 acts genetically downstream of MPK3. Moreover, the
464 loss of the enhanced photosynthetic performance observed in *mpk3 ko* plants upon ACTPK1
465 disruption highlights a linear regulatory hierarchical, in which MPK3 negatively regulates
466 photosynthesis by suppressing ACTPK1 activity.

467 To tie this to RbcS regulation, we used Phos-tag SDS–PAGE to access RbcS phosphorylation
468 across these genotypes. Phos-tag analysis revealed a distinct mobility shift of RbcS in WT and
469 *ACTPK1 OE* seedlings, indicative of phosphorylation. In contrast, no shift was detected in
470 *actpk1 ko* or *mpk3actpk1 ko* seedlings, demonstrating that enhanced RbcS phosphorylation in
471 *mpk3 ko* plants is due to the presence of ACTPK1, thus placing ACTPK1 downstream in this
472 cascade (Fig. 6H). This hierarchy aligns with our biochemical evidence that MPK3
473 phosphorylates ACTPK1 thereby inhibiting its kinase activity and preventing ACTPK1-
474 mediated phosphorylation of RbcS.

475 **Enhanced photosynthetic capacity in ACTPK1 translated to enhanced biomass**

476 Photosynthetic efficiency directly influences plant productivity, where enhanced carbon
477 assimilation supports plant growth and biomass. We next examined the effect of ACTPK1-
478 mediated photosynthesis regulation on plant growth and development. *ACTPK1 OE* and WT
479 seedlings exhibited enhanced shoot and root length compared to *actpk1 ko* which displayed
480 retarded growth, indicating robust vegetative growth fuelled by increased carbon fixation
481 (Supplemental Fig. S9A-C). At maturity, plant height, tiller number per plant, and plant
482 biomass were significantly reduced in *actpk1 ko* lines relative to *ACTPK1 OE* and WT (Fig.
483 7A-D). Moreover, striking differences were observed in flag leaf angle, *ACTPK1 OE* plants
484 displayed highly erect flag leaves with narrow angles (8°–19°), WT plants had moderately open
485 leaves (14°–29°), whereas *actpk1 ko* lines exhibited leaves with widest angles (45°–75°)
486 (Supplemental Fig. S9D-E). As leaf angle strongly influences light interception, these

differences likely have direct consequences for photosynthetic efficiency. Furthermore, flowering time was markedly delayed in *actpk1 ko* by 10–15 days compared to *ACTPK1 OE* and WT. While WT and *ACTPK1 OE* lines initiated flowering at 80–85 days, *actpk1 ko* plants flowered at approximately 100–105 days after sowing, indicating a potential regulatory role of ACTPK1 in floral transition (Supplemental Fig. S9F). These data suggests that, absence of *ACTPK1* disrupts developmental timing and architecture, likely due to impaired photosynthesis and resource allocation.

Interestingly, *ACTPK1* also affects seed architecture and yield. *actpk1 ko* plants exhibited significantly lower number of panicle per plant compared to *ACTPK1 OE* and WT (Fig. 7E). Lower panicle number resulted in reduced grain yield per plant in *actpk1 ko* plants (Fig. 7F). Interestingly, seeds from *actpk1 ko* plants were not only longer but also wider than those from WT and *ACTPK1* OE lines, resulting in a significantly higher 100-seed weight (Fig. 7G, Supplemental Fig. S9G-I). However, these advantages in seed productivity were offset by a substantial reduction in tiller number and panicle number, traits that are key contributors to overall yield. Thus, while *ACTPK1* knockout promotes the formation of larger and heavier seeds, it concurrently suppresses the production of structures such as tillers and panicles that bears reproductive organs, highlighting its role in balancing the trade-off between seed size and seed number.

Discussion

Studying photosynthesis is paramount not only for unravelling the foundational mechanisms of life on Earth but also for addressing pressing global challenges in food security and climate resilience, particularly in staple crops like rice. Our discovery of a non-canonical MAPK signalling cascade consisting of MPK3-ACTPK1-RbcS signalling module, unveils a new mechanism that uniquely integrates cytoplasmic kinase activity with chloroplast protein import. This study offers a novel perspective on how photosynthetic carbon assimilation can be enhanced for crop productivity.

The novelty lies in identifying MPK3 as a negative regulator that phosphorylates and suppresses the activity of ACTPK1, which in turn phosphorylates RbcS at Thr12. Phosphorylation of RbcS by ACTPK1 ensure its cytosolic stability and efficient chloroplast import, thereby directly controlling Rubisco biogenesis, photosynthetic efficiency and plant biomass (Fig 8). The mechanism explains why *mpk3 ko* lines display enhanced photosynthesis. In the absence of MPK3, ACTPK1 remains active, leading to constitutive RbcS phosphorylation. This boosts RbcS import, elevates Rubisco activity, and increases net CO_2 assimilation by 18-21% under ambient conditions. This is evidenced by higher levels of chlorophyll and carotenoid, stomatal conductance, including carboxylation parameters like *Vcmax*, *J*, and *TPU*. Conversely, MPK3 overexpression mimics stress-like inhibition, reducing net CO_2 assimilation by ~29-31% and lowering CO_2-saturated *Amax*. This directly links the cascade to the observed photosynthetic deficits and highlights how the activation of MPK3 could adaptively downregulate carbon fixation to prioritize resource allocation during environmental challenges.

MPK3, located in the cytoplasm and nucleus, indirectly regulates photosynthesis by modulating RbcS phosphorylation dynamics. Phosphorylation is a well-established regulator of photosynthesis, coordinating processes like light harvesting, energy distribution, and photoprotection (Tikkanen and Aro, 2012; Rochaix, 2014). It also drives chloroplast protein import, where phosphorylation of transit peptides and translocon components enables efficient targeting of nuclear-encoded proteins (Waegemann and Soll, 1996; May and Soll, 2000). Importantly, Rubisco itself is phosphorylated on both large and small subunits. These modifications influence enzyme stability and catalytic efficiency (Houtz et al., 1989;

535 Grabsztunowicz et al., 2017). Loss of RbcS phosphorylation prevents its proper assembly into
536 the holoenzyme, leading to loss of Rubisco function (Kaul et al., 1986). In *mpk3 ko* plants,
537 RbcS phosphorylation is enhanced, which results in sustained RbcS stability, import and
538 Rubisco assembly. This also justifies the enhanced carboxylation efficiency in *mpk3 ko* lines.
539 The discovery that ACTPK1, a kinase homologous to Arabidopsis STY8, STY17 and STY46
540 (Lamberti et al., 2011, Beier et al., 2018), drives RbcS precursor import in chloroplast unveils
541 a critical regulatory mechanism. Thus, positioning ACTPK1 as the pivotal link that translates
542 cytoplasmic MPK3 signalling into RbcS phosphorylation dynamics. This mechanism
543 integrates seamlessly into a broader regulatory network, connecting cytoplasmic cues to
544 chloroplast function under normal conditions.

545 The physical and functional interaction between MPK3 and ACTPK1 further integrates these
546 findings by linking MAPK signalling to chloroplast protein trafficking. Y2H, BiFC, and Co-
547 IP assays confirm their direct association, while *in vitro* kinase assays reveals unidirectional
548 phosphorylation of ACTPK1 by MPK3. This kinase-on-kinase phosphorylation represents a
549 conserved regulatory mechanism in plant signalling networks, where post-translational
550 modifications—such as reversible phosphorylation by kinases—modulate target kinase activity
551 to fine-tune responses to environmental cues, including nutrient availability and stress (Manna
552 et al., 2023). Specifically, MPK3-mediated phosphorylation inhibits ACTPK1, as evident by
553 reduced MBP phosphorylation in WT immunoprecipitants compared to *mpk3 ko* in IP-kinase
554 assay. Such inhibition mirrors MPK3's role in stabilizing downstream targets like KRP3
555 through phosphorylation to regulate plant growth, but in this context MPK3 exerts inhibitory
556 control via MAPK cascades (Banerjee et al., 2025). Consequently, this suppression limits RbcS
557 phosphorylation in WT plants, promoting cytosolic degradation and impairing chloroplast
558 import. Conversely, active ACTPK1 in *mpk3 ko* enables sustained RbcS phosphorylation,
559 enhancing precursor stability, translocation efficiency, and assembly of functional Rubisco.
560 This mechanism boosts photosynthetic rates, akin to observations in MAPK-regulated carbon
561 fixation pathways, including the OsMPKK10.2-OsMPK6 cascade that phosphorylates factors
562 for defence and metabolism (Ma et al., 2021). Thus, MPK3 fine-tunes RbcS trafficking to
563 balance photosynthetic capacity, with *mpk3 ko* exhibiting elevated CO_2 assimilation rates under
564 normal conditions, underscoring the cascade's role in optimizing carbon fixation and plant
565 fitness.

566 Moreover, gain- and loss- of function phenotypes of ACTPK1 reveal interconnected roles in
567 rice development and yield. Specifically, *actpk1 ko* exhibit retarded growth, delayed flowering,
568 reduced tillers and panicles which collectively impair overall plant productivity. This
569 phenotype is rationalized by ACTPK1's regulation of ammonium uptake through modulation
570 of high-affinity AMT1 transporters; under sufficient ammonium, ACTPK1 phosphorylates and
571 inactivates AMT1;2, limiting uptake to prevent toxicity, whereas its loss enhances uptake but
572 disrupts balanced nutrition (Beier et al., 2018). Optimal ammonium nutrition promotes erect
573 leaves, enhanced chlorophyll content, protein synthesis, photosynthesis, tillering, and seed
574 filling (Shilpha et al., 2023). This provides a mechanistic basis that the developmental deficits
575 in ACTPK1 absence might be due to altered nitrogen assimilation and resource allocation. In
576 our study, *actpk1 ko* plants displayed wider flag leaf angles correlating with 36-45% lower
577 assimilation rates, reduced *gs*, and diminished *Vcmax*, *J*, and *TPU,* compared to erect leaves
578 and maintained photosynthetic efficiency of *ACTPK1 OE* plants. Plant hormones, including
579 brassinosteroids (BRs), auxins, and gibberellins, regulate leaf angle, with BRs exerting the
580 dominant influence by coordinating cell expansion and mechanical tissue formation at the
581 lamina joint (Luo et al., 2016, Nolan et al., 2020). Disruptions in BR signalling typically result
582 in erect leaves and smaller seeds, while enhanced signalling promotes wider angles and larger
583 seeds, suggesting ACTPK1's potential integration into BR pathways to balance architecture

584 and reproduction. However, a rice homologue of ACTPK1, Increased Leaf Angle 1 (ILA1, also
585 known as ACTPK4), controls leaf angle via mechanical tissue regulation in a BR-independent
586 manner (Ning et al., 2011), indicating pathway divergence and necessitating further studies for
587 a clear picture. Rice grain size is governed by cell proliferation and expansion during
588 organogenesis, involving interconnected pathways such as G-protein signalling, ubiquitin-
589 proteasome degradation, MAPK cascades, BR responses, transcriptional regulators, and auxin
590 signalling (Li et al., 2019). For instance, MPKKK10/55/60/70 modulate flag leaf angle and
591 seed size through canonical MAPK cascades (Guo et al., 2018; Liu et al., 2021), providing a
592 framework for how ACTPK1, as part of similar signalling, might influence these traits.
593 Additional research is required to elucidate ACTPK1's direct role in grain size control and its
594 interacting partners, as current evidence points to indirect effects via disrupted development.
595 Overall, our study highlights the importance of ACTPK1 in optimizing rice architecture for
596 enhanced carbon capture. Efficient RbcS import in *ACTPK1 OE* or *mpk3 ko* supports robust
597 carbon assimilation, supplying resources for vegetative and reproductive growth. However,
598 ACTPK1 loss disrupts this, leading to yield trade-offs like larger seeds but fewer panicles.
599 Thus, MPK3-mediated inhibition of ACTPK1 not only suppresses photosynthesis but also
600 indirectly modulates growth and yield, emphasizing the holistic impact of this cascade on rice
601 fitness.

602 At the molecular interface, ACTPK1 phosphorylates RbcS at Thr12 in its signal peptide, as
603 confirmed by *in vitro* kinase assays and site specific mutation studies. This modification
604 stabilizes RbcS against rapid degradation and promotes efficient chloroplast targeting.
605 $RbcS^{T12D}$ (Phospho-mimic) aggregate outside chloroplast while $RbcS^{T12A}$ (phospho-dead)
606 show partial dual localization, consistent with studies on transit peptide phosphorylation aiding
607 recognition and dephosphorylation enabling translocation (Waegemann and Soll, 1996; May
608 & Soll, 2000; Lee et al., 2009). However, the absence of RbcS–GFP signal in *actpk1*
609 protoplasts, together with its rapid loss in degradation assays, reveals a protective role of
610 ACTPK1 beyond import regulation. In its absence, newly synthesized RbcS is rapidly degraded
611 by degradation pathways. These findings suggest that ACTPK1 stabilizes RbcS precursors,
612 likely by maintaining them in an import-competent state through phosphorylation. This
613 connects to the enhanced Rubisco activity in *mpk3 ko*, where uninhibited ACTPK1 ensures
614 high RbcS import, boosting carboxylation and explaining the *mpk3 ko* superior *A/Ci* responses.
615 While in ACTPK1-deficient plants, failed import causes RbcS degradation, reduced Rubisco,
616 and photosynthetic collapse, highlighting the reliance of the cascade on this site-specific
617 phosphorylation event.

618 Genetic epistasis solidifies the linear hierarchy within this signalling module. The *mpk3actpk1*
619 double mutant shows a complete loss of RbcS phosphorylation and phenocopies *actpk1 ko* in
620 its reduced CO_2 assimilation, and Rubisco activity. Notably, it also fails to exhibit the enhanced
621 photosynthesis observed in *mpk3 ko,* demonstrating that ACTPK1 functions downstream of
622 MPK3 and that the cascade's integrity is essential for photosynthetic regulation. This epistatic
623 relationship integrates all observations—MPK3's inhibition prevents ACTPK1-mediated RbcS
624 phosphorylation, import, and stability, directly causing the photosynthetic phenotypes.
625 Together, the results positions the MPK3-ACTPK1 module as an adaptive regulatory switch:
626 under non-stress conditions, hypoactive MPK3 allows ACTPK1 to sustain photosynthesis,
627 whereas stress induced MPK3 activation supresses ACTPK1, blocks RbcS import, degrade
628 precursor of RbcS, and reallocates carbon to balance trade-offs between efficiency and
629 resilience. Unlike previously described context-dependent MAPK effects, our findings reveals
630 a conserved and fundamental mechanism of basal photosynthetic regulation, with rice-specific
631 features providing additional insights into species-specific adaptative fine-tuning.

632

633 **Materials and Methods**

634 **Transgene construct**

635 For generation of overexpression lines, full-length coding sequence (CDS) of *ACTPK1* was
636 amplified with 3xFLAG tag at 5' end and 4xMYC tag at 3' end was sandwiched between 35S
637 promoter and Nos terminator and cloned into binary vector pCAMBIA1300-CaMV 35S. The
638 pCAMBIA1300-35S-*ACTPK1* plasmid was introduced into rice *japonica* cultivar Taipea309
639 (Tp309) via *Agrobacterium*-mediated transformation using *Agrobacterium* strain EHA105.

640 *ACTPK1* knockout mutants were generated using CRISPR-Cas9 mediated gene editing in
641 japonica cultivar Tp309 background according to Rengasamy et al., 2024. A single guide RNA
642 (sgRNA) targeting the CDS region of *ACTPK1* gene (sgRNA:
643 GGGGACGGCGCGCGGACAAGAGC, PAM sequence: GGG) was designed and
644 synthesized as an oligonucleotide. The synthesized sgRNA was then cloned in pRGB32 vector
645 and introduced into 10-day-old rice Calli through *Agrobacterium*-mediated transformation.
646 The *MPK3-ACTPK1* double knockout was generated by mutating *ACTPK1* in *mpk3 ko*
647 background using CRISPR-Cas9 genome editing tool using the same sgRNA (sgRNA:
648 GGGGACGGCGCGCGGACAAGAGC).

649 **Plant growth conditions**

650 Rice seeds used for photosynthesis experiments were homozygous seeds of atleast T2
651 generation. Along with *ACTPK1 OE*, *actpk1 ko* and *mpk3-actpk1* double knockout,
652 dexamethasone (DEX) inducible MPK3 OE lines (*MPK3-23*, *MPK3-24*) and *mpk3 ko* (*mpk3*
653 *ko1*, *mpk3 ko2*) plants (both generated in *Oryza sativa* Tp309 cultivar) were used (Singh et al
654 2019, Banerjee et al., 2025). Seeds were germinated in petri plates having moist germination
655 paper for 7 days at 28 ºC, 16h light and 8h dark conditions. Seven days old seedlings were
656 transferred to one-fourth M.S. (Himedia) hydroponics media containing both micro and
657 macronutrients. The pH of the media solution was adjusted to 5.5, and media was renewed
658 every 3 days. Post 20 days, plants were transferred to pots and kept in a greenhouse at 28/22
659 ºC day and night air temperature, 70% relative humidity, a photoperiodic cycle of 16h light/8h
660 dark photoperiod, and ~500 µmol m^{-2} s^{-1} light intensity. The plants were maintained in pots in
661 greenhouse until maturity, and photosynthetic parameters were recorded from the middle
662 widest area of flag leaf at heading stage. For *MPK3 OE* lines, 1 um DEX and DMSO (mock)
663 were sprayed one day prior to taking photosynthetic readings (Singh et al., 2019).

664 **Photosynthesis rate and related physiological trait measurements**

665 Photosynthetic rate and its related physiological parameters were measured using Li-COR 6800
666 portable photosynthesis system on the flag leaf of rice plant at heading stage. The area of Li-
667 COR 6800 portable system leaf chamber was set at 2 cm^2 with a LED light source (LI-6400-
668 02B; LI-COR, Inc). To acquire the same leaf area, two young leaves were carefully placed in
669 leaf chamber without any overlap for plants having leaf width less than 2 cm^2 (Busch et al,
670 2018). For all the measurements, the conditions of leaf chamber were set as follows: 1500 µmol
671 m^{-2} s^{-1} light intensity (PAR), 400 µmol mol^{-1} CO_2 concentration, 300 µmol s^{-1} constant airflow,
672 70-80% relative humidity. Ten flag leaves from different plants were used to evaluate the net
673 photosynthesis rate (*A*), intercellular CO_2 concentration (*Ci*) and stomatal conductance to water
674 (*gs*).

675 For A/Ci curve, the leaves were first acclimatised to ambient CO_2 concentration of 400 µmol
676 mol^{-1} CO_2 and a constant PAR of 1500 µmol m^{-2} s^{-1} for 10 min and then the CO_2 concentration
677 was first gradually decreased from 400 to 50 (400, 300, 200, 150, 100, 50) µmol mol^{-1} CO_2 and
678 then leaf was stabilized at 400 µmol mol^{-1} CO_2 and again CO_2 concentration was increased

679 from 400 to 1400 (400, 600, 800, 1000, 1200 and 400) µmol mol^{-1} CO_2. The minimum and
680 maximum wait time between the subsequent readings was 60 and 120 sec respectively.
681 Readings were taken at constant PAR of 1500 µmol m^{-2} s^{-1}, flow rate of 500 µmol s^{-1}. The
682 maximum rate of Rubisco mediated carboxylation (*Vcmax*), electron transport rate (*J*) and
683 triose phosphate utilisation (*TPU*) were calculated by fitting A/Ci curve using Farquhar-von
684 Caemmerer-Berry (FvcB model) (Sharkey, 2015).

685 For light curve, the leaf was first acclimatised to constant saturating photosynthetic active
686 radiation (PAR) of 1500 µmol m^{-2} s^{-1} for about 10 min and then the PAR was decreased from
687 1500 to 100 (1500,1200,1000, 700, 500, 300 and 100) µmol m^{-2} s^{-1} at constant CO_2
688 concentration of 400 µmol mol^{-1} CO_2 and flow rate of 500 µmol s^{-1}. The minimum and
689 maximum wait time between the subsequent readings was 120 and 180 sec respectively.

690 All measurements were taken between 9.00 am to 11.00 am.

691 **Gene expression analysis**

692 Total RNA was isolated from leaf samples using RNeasy Plant mini kit (Qiagen) following
693 manufacturer's protocol. DNase treatment was given to 2 µg RNA using RNA free DNase I
694 (Qiagen) and subjected to first strand cDNA synthesis using RevertAid First Strand cDNA
695 synthesis kit (Thermo Scientific) per the manufacturer's protocol. Quantitative RT-PCR of
696 ACTPK1 was carried out using Power SYBR Green PCR master mix (Applied Biosystems).
697 The conditions of thermocycler were set as follows: 94 °C for 10 min, 40 cycles of 94 °C for
698 20 sec, 60 °C for 1 min. The housekeeping gene UBQ5 and Actin7 were used as an internal
699 control for normalization. Expression levels of examined genes were quantified using relative
700 quantitation method (ΔΔCT). The statistical significance was evaluated using t-test. Data
701 shown is the mean value of at least three biological repeats with SD. The primers used for
702 doing qRT-PCR are listed in supplemental Table 1.

703 **Site-directed mutagenesis**

704 Site-directed mutagenesis was performed using overlap extension PCR. Complementary
705 primers containing the desired mutation were designed. The target gene was amplified in two
706 fragments using gene-specific forward and mutation-specific reverse primers, and mutation-
707 specific forward and gene-specific reverse primers. Both amplicons were gel-purified and used
708 in overlap extension PCR with the following conditions: 98°C for 30 s, 55–58°C for 1 min,
709 72°C for 30 s/kb for 10 cycles. Gene-specific primers were then added for 35 additional cycles.
710 The final PCR product was gel-purified, verified by DNA sequencing, and cloned into the
711 target vector.

712 **Bacterial protein induction, purification and *in vitro* phosphorylation assay**

713 The full length CDS of *MPK3*, *MPK6*, *ACTPK1*, and *RbcS* were cloned in-frame with the
714 sequence of GST-tag in pGEX4-T-2 vector. Recombinant protein was induced in *Escherichia*
715 *coli BL21 Rosetta®* by adding 1mM IPTG at 22 °C. Induced recombinant proteins with GST-
716 tag were purified by affinity chromatography using GST-sepharose beads. Protein
717 concentration was determined using Bradford reagent (Sigma) and purity was analysed using
718 SDS-PAGE. *In vitro* phosphorylation assay was performed according to the method described
719 by Raghuram *et al*, 2015. Briefly, purified recombinant proteins of kinase and substrate (ratio
720 1:10) were incubated in kinase reaction buffer (25 mM Tris/Cl (pH 7.5), 10 mM $MgCl_2$, 5 mM
721 $MnCl_2$, 1 mM DTT, 1 mM β-glycerol phosphate, 1 mM Na_3VO_4, 25 mM ATP and 1 mCi [γ-
722 32P] ATP) for 30 min at 30 °C. The reaction was stopped by adding 6X SDS sample buffer
723 followed by heating at 95 °C for 5 min. The reaction samples were subjected to 12% SDS-

724 PAGE and exposed to phosphor screen followed by visualization using phosphor imager
725 (Typhoon, Phosphor Imaging System, GE Health Care, Life Sciences).

726 **Plant protein extraction and Immunoblot Analysis**

727 Proteins were extracted from rice seedlings using protein extraction buffer (50 mM Tris HCl
728 (pH 7.5), 5 mM EDTA, 5 mM EGTA, 150 mM NaCl, 1 mM DTT, 10 mM Na_3VO_4, 10 mM
729 NaF, 1mM PMSF, 10% glycerol (v/v), 0.1% Nonidet P-40 (v/v) and 1× protease inhibitor
730 cocktail (Sigma-Aldrich/Merck)). Extracted proteins were quantified with Bradford reagent
731 and ~40 µg was separated by 10/12% SDS-PAGE. Separated proteins were transferred to
732 PVDF membrane for immunodetection. The membranes were first blocked with 5% skimmed
733 milk in TBST (10 mM Tris (pH 7.5), 500 mM NaCl, 0.05% Tween 20) for 2 h, then probed
734 with anti RbcS (Agrisera, dilution 1:5000), anti Actin (Sigma-Aldrich, dilution 1:5,000)
735 antibody in TBST for 2 h at room temperature. After two TBST washes (2 min each),
736 membranes were incubated with anti-rabbit secondary antibody (Thermo Fisher Scientific
737 A11034) for 1.5 h. The membrane was again washed twice with TBST (10 min each) and MQ
738 water, and visualized using Immobilon Western chemiluminescent HRP substrate (BIORAD)
739 as per manufacturer's instructions. Chemiluminescence was detected with ChemiDoc system
740 iBright 1500 (Amersham Biosciences).

741 ***In vivo* phosphorylation assay**

742 *In vivo* phosphorylation of RbcS was examined by mobility shift assay employing phos-tag
743 reagent. Proteins were extracted from WT, *mpk3 ko, ACTPK1 OE, actpk1 ko, mpk3actpk1 ko*
744 seedlings using protein extraction buffer (50 mM Tris HCl (pH 7.5), 150 mM NaCl, 1 mM
745 DTT, 10 mM NaF, 1mM PMSF, 10% glycerol (v/v) and 0.1% Nonidet P-40 (v/v)). Extracted
746 protein was separated by 12% (w/v) SDS-PAGE gel containing 100 µM phos-tag and 100 mM
747 $MnCl_2$. After electrophoresis, the gel was washed thrice, twice with transfer buffer containing
748 10 mM EDTA and once without EDTA for 10 min. Post washing, separated proteins were
749 transferred to nitrocellulose membrane using Trans-Blot SD cell (BIO-RAD) and membrane
750 was probed with α-RbcS (Agrisera) antibody. The membrane was again washed twice with
751 TBST (10 min each) and MQ water, and visualized using Immobilon Western
752 chemiluminescent HRP substrate (BIORAD) as per manufacturer's instructions.
753 Chemiluminescence was detected with ChemiDoc system iBright 1500 (Amersham
754 Biosciences).

755 **Immuno-kinase (IP-kinase) assay**

756 Total protein was extracted from the 14 day old seedlings of WT, *mpk3 ko1* and *mpk3 ko2*
757 using the previously described protein extraction. Extracted proteins were quantified using
758 Bradford reagent, and 1 mg crude protein was incubated with 5 µg anti ACTPK1 antibody
759 (genescript) on a rocker at 4°C for 3 h. Subsequently, 50 µL Protein A Sepharose beads (50%
760 slurry, Pierce) were added and incubated on a rocker at 4°C for 1.5 h. Post incubation,
761 sepharose beads were washed with PBS-T (PBS with 0.05% Tween 20) thrice, resuspended in
762 kinase buffer containing 1 mCi [γ-^{32}P] ATP and 0.5 µg MBP, and incubated at 30°C for 30
763 min. Reactions were stopped with 3× SDS dye, boiled at 95°C for 5 min, and resolved by 12%
764 SDS-PAGE. Gels were exposed to a phosphor screen and visualized using a Typhoon phosphor
765 imager (GE Healthcare).

766 **Yeast two-hybrid assay**

767 The interaction between MPK3 and ACTPK1, and ACTPK1 and RbcS was examined using
768 the Matchmaker Gold Yeast Two-hybrid System (Takara Bio). Full-length CDS of MPK3,
769 MPK6, ACTPK1 and RbcS were cloned in pGBKT7 and pGADT7 vector (Clontech). Yeast

770 transformation with was performed using Fast Yeast Transformation kit (Gbiosciences; GZ-1)
771 (according to the manufacturer's protocol). The positive transformants were selected on double
772 dropout medium (Synthetic Defined (SD) /-Leu/-Trp)). The interaction assay was performed
773 by plating the selected transformants on quadruple dropout medium ((SD)/-Ade/-His/-Leu/-
774 Trp) followed by incubation at 30 °C for 36–48h. The fully grown colonies after the incubation
775 were marked as positive interactions.

776 **Subcellular localisation and Bimolecular Fluorescence Complementation assay (BiFC)**

777 For subcellular localisation, full-length CDS of MPK3 and RbcS was cloned in pGWB5 vector.
778 The resulting construct (MPK3-pGWB5) was transformed into *Agrobacterium* strain EHA105
779 and infiltrated in young and healthy leaves of *Nicotiana benthamiana*. The plasmid of RbcS-
780 pGWB5, $RbcS^{T12D}$-pGWB5 and $RbcS^{T12A}$-pGWB5 was introduced in rice protoplast using
781 PEG-mediated transformation (citation). Localisation was analysed post 48h for *Nicotiana*
782 *benthamiana* and post 16h for rice protoplast using a Leica TCS SP8 AOBS Laser Scanning
783 Microscope (Leica Microsystems) using GFP filters with fluorescence excitation at 514 nm
784 and emission at 527 nm.

785 For BiFC, full length CDS of MPK3, ACTPK1 and RbcS was cloned into pSITE-nEYFP-C1
786 (Cd3-1648) and pSITE-cEYFP-N1 (Cd3-1651) vectors. The resulting constructs were
787 transformed into *Agrobacterium* strain EHA105 and infiltrated in young and healthy leaves of
788 *Nicotiana benthamiana*. Interaction was analysed post 48h using a Leica TCS SP8 AOBS Laser
789 Scanning Microscope (Leica Microsystems) using YFP filters with fluorescence excitation at
790 514 nm and emission at 527 nm.

791 **Co-immunoprecipitation (Co-IP) assay**

792 Flag-tagged ACTPK1 (pCAMBIA1300-35S-Flag-*ACTPK1*) and GFP-tagged MPK3 (MPK3-
793 pGWB5) were co-expressed in *Nicotiana benthamiana* leaves via *Agrobacterium*-mediated
794 infiltration. Proteins were extracted 48 h post-infiltration using protein extraction buffer.
795 Proteins (1 mg) were incubated with 5 µg anti-Flag antibody (Sigma-Aldrich) at 4°C for 3 h
796 with rocking, followed by 50 µL Protein A Sepharose beads (50% slurry, Pierce) for 1.5 h.
797 Beads were washed thrice with PBS-T (PBS, 0.05% Tween 20), eluted with 2× SDS sample
798 buffer, boiled at 95°C for 5 min, and resolved on 10% SDS-PAGE. Proteins were transferred
799 to PVDF, blocked with 5% skimmed milk in TBST (10 mM Tris, pH 7.5; 500 mM NaCl; 0.05%
800 Tween 20) for 2 h, and probed with anti-GFP antibody (Abcam) for 2 h at room temperature.
801 After two 10-min TBST washes, membranes were incubated with HRP-conjugated secondary
802 antibody for 1.5 h, washed twice with TBST and MQ water, and visualized using Immobilon
803 Western chemiluminescent HRP substrate (BIORAD) as per manufacturer's instructions.
804 Chemiluminescence was detected with ChemiDoc system iBright 1500 (Amersham
805 Biosciences).

806 **Cell-free degradation assay**

807 Total protein was extracted from 14-day-old rice seedlings (WT, *mpk3 ko*, *actpk1 ko*) by
808 grinding 1 g tissue in liquid nitrogen and homogenizing in 1 mL ice-cold protein extraction
809 buffer. Extracted proteins were quantified using Bradford reagent. Crude extract (100 µg) was
810 incubated with 1 µg recombinant GST-tagged RbcS in 100 µL reaction buffer (50 mM Tris-
811 HCl, (pH 7.5), 5 mM $MgCl_2$, 5 mM ATP, and 1 mM DTT) at room temperature. Aliquots (20
812 µL) were collected at 0, 5, 10, 30, 60, and 120 min, stopped with 2× SDS sample buffer, boiled
813 at 95°C for 5 min, and resolved on 12% SDS-PAGE. Proteins were transferred to nitrocellulose
814 membrane and probed with anti-GST antibody (Thermofischer), and visualized using
815 Immobilon Western chemiluminescent HRP substrate (BIORAD) as per manufacturer's

816 instructions. Chemiluminescence was detected with ChemiDoc system iBright 1500
817 (Amersham Biosciences). Band intensity was quantified with ImageJ.

818 **Rubisco activity measurements**

819 Rubisco activity assay was performed according to Sharwood et al., (2016). Briefly, Leaf
820 tissues were excised (2 cm^2) from the middle widest part of the same leaf from which
821 photosynthesis parameters were recorded, pulverized and homogenized in 1 mL ice-cold
822 extraction buffer (5 mM DTT, 10 mg ml^{-1} PVPP, 2 mg ml^{-1} BSA, 2 mg ml^{-1} PEG, 2% (v/v)
823 Tween-80, 12 mM 6-aminocaproic acid, 2.4 mM benzamidine in HEPES stock) at 4 °C. The
824 homogenate was centrifuged at 15,000 × g at 4°C for 1 min, and supernatant was incubated
825 with freshly prepared BMEC buffer (100 mM Bicine–NaOH, pH 8.2, 20 mM $MgCl_2$, 1 mM
826 Na_2-EDTA, and 10 mM $NaHCO_3$) in a 9:1 ratio (e.g. 900 µl leaf extract to 100 µl BMEC) at
827 25 °C for 25 min, to activate the Rubisco enzyme. To assess the activity, 50 µl of leaf extract
828 was incubated with 1550 µl of EME buffer (100 mM EPPS–NaOH (pH 8.2), 20 mM $MgCl_2$, 1
829 mM Na_2-EDTA), 40 µl of 10 mM NADH (final concentration 200 µM), 80 µl of 250 mM
830 $NaH_{12}CO_3$ (final concentration 10 mM), 200 µl of ATP/phosphocreatine (final concentrations
831 1 mM and 5 mM, respectively), 40 µl of coupling enzymes (carbonic anhydrase 500 U,
832 glyceraldehyde-3-phosphate dehydrogenase 50 U, 3-phosphoglycerate kinase 50 U, triose-
833 phosphate isomerase/glycerol-3-phosphate dehydrogenase 400/40 U), and 40 µl of 25 mM
834 RuBP (final concentration 500 µM), and the decrease of absorbance was monitored at 340 nm
835 for 180 s using a UV–Vis spectrophotometer. The Rubisco carboxylation rate was calculated
836 using the equation:

837 RuBP− use (µmol s^{-1}) = (ΔOD340 ∗ Vol)/6.18 X 4

838 assuming an extinction coefficient of 6.18 µmol ml^{-1} cm^{-1} for NADH oxidation at 340 nm.
839 ΔOD340 is the rate of change of absorbance at 340 nm per second, and Vol is assay volume (1
840 ml). The equation accounts for the four NADH molecules oxidized per RuBP carboxylated by
841 Rubisco. The activity of Rubisco (*Vcmax*) is calculated as:

842 *Vcmax* (µmol m^{-2} s^{-1}) = ((RuBP−use; µmol s^{-1}) (EV; µl) (10000 cm^2/m^2))/(LA; cm^2) (Sample
843 volume; µl)

844 where EV is extraction volume and LA is leaf area.

845 **Rice protoplast isolation and PEG mediated transformation**

846 Protoplast from rice seedlings were isolated according to Zhang et al., 2011. Seeds of WT,
847 *mpk3 ko* and *actpk1 ko* were surface sterilized and germinated on half-strength MS solid
848 medium. Seven- to ten-day-old seedlings were chopped into 0.5 mm strips in 0.5 M mannitol,
849 incubated for 10 min, and transferred to enzyme solution (0.4 M mannitol, 1.5% Cellulase RS
850 (Yakult), 0.75% Macerozyme (Yakult), 20 mM MES (pH 5.7), 10 mM $CaCl_2$, 20 mM KCl,
851 0.1% BSA) for 3-4 h at 80 rpm at room temperature. The reaction was stopped with equal
852 volume of W5 buffer (154 mM NaCl, 125 mM $CaCl_2$, 5 mM KCl, 2 mM MES (pH 5.7)),
853 shaken for 10 s to release protoplasts, and filtered through a 100 µm nylon mesh. Additional 5
854 ml W5 buffer was added to the strips, strained again and centrifuged at 1500 rpm for 3 min at
855 room temperature. The pellet was washed with 5 mL W5 buffer, resuspended in MMG buffer
856 (4 mM MES (pH 5.7), 0.4 M Mannitol, 15 mM $MgCl_2$), and protoplast quality was assessed
857 under a light microscope.

858 PEG-mediated transient transformation of protoplasts was performed according to Shen et al.,
859 (2014). Approximately 100 µL of protoplasts were mixed with 5–10 µg plasmid of RbcS-
860 pGWB5, $RbcS^{T12D}$-pGWB5 and $RbcS^{T12A}$-pGWB5 in a microcentrifuge tube by gentle
861 tapping. Subsequently, 110 µL of PEG solution (40% PEG_{4000} (Fluka), 0.2 M Mannitol, 100

mM $CaCl_2$) was added, mixed by tapping, and incubated in the dark at room temperature for 20 min. The solution was diluted with 440 µL W5 buffer, centrifuged at 1500 rpm for 3 min, and the pellet was resuspended in 1 mL WI solution (4 mM MES, 0.5 M mannitol, 20 mM KCl). After 16 h incubation in the dark, transformed protoplasts were analysed using a Leica TCS SP8 AOBS Laser Scanning Microscope (Leica Microsystems) using GFP and chloroplast autofluorescence filters.

Pigment content measurement

Pigment content were measured according to procedure described by Porra et al., (1989). Leaf samples (1 g) were harvested post photosynthetic parameters measurements, and chlorophyll and total carotenoid was extracted in 80% ice-cold acetone (aqueous). Chlorophyll and carotenoid contents were measured spectrophotometrically and calculated according to Arnon, 1949.

Statistical analysis

Student t-test and one-way analysis of variance (ANOVA) were performed to determine significant differences indicated as *P<0.05, **P< 0.005, and ***P< 0.0005. Details of statistical analysis and sample sizes in each experiment are mentioned in the figure legends. ImageJ was used to quantify the intensities of bands in the immunoblots.

Supplemental figure and table legends:

Fig S1. Photosynthetic pigments and parameters in WT, *MPK3 OE* (*MPK3-23*, *MPK3-24*) and *mpk3 ko* (*mpk3 ko1*, *mpk3 ko2*) lines.

Fig. S2 Localisation of MPK3 and interaction and phosphorylation of RbcS with MPK3 and MPK6.

Fig. S3 ACTPK1 is a Raf-like MAPKKK exhibiting homology and sequence similarity with *At*STY8, *At*STY17 and *At*STY46, and contains multiple MAPK phosphorylation motifs.

Fig. S4 Lysine at 332 and 428 are crucial for trans- and auto-phosphorylation activity of ACTPK1 and ACTPK1 do not phosphorylate MPK3.

Fig. S5 ACTPK1 phosphorylates RbcS at Thr12.

Fig. S6 Absence of RbcS-GFP signal in *actpk1 ko* protoplasts.

Fig. S7 Development of *ACTPK1 OE* and *actpk1 ko* lines.

Fig. S8 Intercellular CO_2 concentration in flag leaf of WT, *ACTPK1 OE* and *actpk1 ko* plants.

Fig. S9 ACTPK1 regulates vegetative growth, flag leaf angle, flowering time and seed architecture.

Supplemental Table1: Table containing the list of primers used in this study.

Acknowledgments

SJ and RB are thankful to the Department of Biotechnology (DBT) for the fellowship. GB and PS are thankful to the Council of Scientific and Industrial Research (CSIR) for the fellowship. AKS thanks Sir JC Bose Fellowship from the Anusandhan National Research Foundation, Department of Science and Technology, Government of India (File no.: JCB/2020/000041). The work is supported by the grant from the Anusandhan National Research Foundation, Department of Science and Technology, Government of India (File No.: CRG/2023/001751). The authors also acknowledge the Gene Functional Analysis Platform for Crops, Confocal Facility, DNA sequencing facility, Radioisotope facility and the Central Instrumentation Facility of NIPGR, New Delhi, India. The authors declare no conflict of interest.

Authors' contribution

SJ and AKS planned the study and designed the experiments. SJ and GB carried out the molecular biology experiments. SJ and RB generated and screened transgenic plants and recorded the photosynthetic parameters. SJ and MM recorded and analysed the phenotypic traits of transgenic plants. PS screened the *mpk3actpk1* double knockout plants. SJ and AKS analysed data and wrote the manuscript. SJ wrote the initial draft and AKS finalise the draft. All authors read and approved the final manuscript.

Declaration of competing interest

The authors declare no competing interests.

References:

Allen, D. J., & Ort, D. R. (2001). Impacts of chilling temperatures on photosynthesis in warm-climate plants. *Trends in plant science*, *6*(1), 36-42.

Andersson, I., & Backlund, A. (2008). Structure and function of Rubisco. *Plant Physiology and Biochemistry*, *46*(3), 275-291.

Arnon, D. I. (1949). Copper enzymes in isolated chloroplasts. Polyphenoloxidase in Beta vulgaris. *Plant physiology*, *24*(1), 1.

Banerjee, G., Jonwal, S., Pal, U., Rengasamy, B., Singh, D., & Sinha, A. K. (2025). Phosphorylation of KRP3, a KIP-related protein by MPK3 modulates rice tiller and seed number by fine-tuning cell division. *Plant biotechnology Journal (in press)*.

Beier, M. P., Obara, M., Taniai, A., Sawa, Y., Ishizawa, J., Yoshida, H., ... & Hayakawa, T. (2018). Lack of ACTPK 1, an STY kinase, enhances ammonium uptake and use, and promotes growth of rice seedlings under sufficient external ammonium. *The Plant Journal*, *93*(6), 992-1006.

Bellafiore, S., Barneche, F., Peltier, G., & Rochaix, J. D. (2005). State transitions and light adaptation require chloroplast thylakoid protein kinase STN7. *Nature*, *433*(7028), 892-895.

Bruce, B. D. (2000). Chloroplast transit peptides: structure, function and evolution. *Trends in cell biology*, *10*(10), 440-447.

Busch, F. A., Sage, R. F., & Farquhar, G. D. (2018). Plants increase CO2 uptake by assimilating nitrogen via the photorespiratory pathway. *Nature plants*, *4*(1), 46-54.

Carrera, A. C., Alexandrov, K., & Roberts, T. M. (1993). The conserved lysine of the catalytic domain of protein kinases is actively involved in the phosphotransfer reaction and not required for anchoring ATP. *Proceedings of the National Academy of Sciences*, *90*(2), 442-446.

Eichberg, J., & Iyer, S. (1996). Phosphorylation of myelin proteins: recent advances. *Neurochemical research*, *21*(4), 527-535.

Evans, J. R. (2013). Improving photosynthesis. *Plant physiology*, *162*(4), 1780-1793.

Evans, J. R. (2021). Mesophyll conductance: walls, membranes and spatial complexity. *New Phytologist*, *229*(4), 1864-1876.

Fabre, D., Yin, X., Dingkuhn, M., Clément-Vidal, A., Roques, S., Rouan, L., ... & Luquet, D. (2019). Is triose phosphate utilization involved in the feedback inhibition of photosynthesis in rice under conditions of sink limitation?. *Journal of Experimental Botany*, *70*(20), 5773-5785.

Farquhar, G. D., von Caemmerer, S. V., & Berry, J. A. (1980). A biochemical model of photosynthetic CO2 assimilation in leaves of C3 species. *planta*, *149*(1), 78-90.

Feiz, L., Williams-Carrier, R., Wostrikoff, K., Belcher, S., Barkan, A., & Stern, D. B. (2012). Ribulose-1, 5-bis-phosphate carboxylase/oxygenase accumulation factor1 is required for holoenzyme assembly in maize. *The Plant Cell*, *24*(8), 3435-3446.

Gao, J., Li, S., Lei, Y., Wang, Q., Ning, Z., Lu, Z., ... & Yang, W. (2024). Delayed photosynthesis response causes carbon assimilation reduction in soybean under fluctuating light. *Journal of Integrative Agriculture*.

Gao, X., Xin, D., Zhao, Y., Li, J., Cao, Y., Zhang, S., & Guo, J. (2024). Potential molecular mechanism of photosynthesis regulation by PeMPK7 in poplar under para-hydroxybenzoic acid stress. *Ecotoxicology and Environmental Safety*, *276*, 116329.

Gawroński, P., Witoń, D., Vashutina, K., Bederska, M., Betliński, B., Rusaczonek, A., & Karpiński, S. (2014). Mitogen-activated protein kinase 4 is a salicylic acid-independent regulator of growth but not of photosynthesis in Arabidopsis. *Molecular Plant*, *7*(7), 1151-1166.

Gibson K, Park JS, Nagai Y, Hwang SK, Cho YC, Roh KH et al (2011) Exploiting leaf starch synthesis as a transient sink to elevate photosynthesis, plant productivity and yields. *Plant science*, *181*(3), 275-281

Grabsztunowicz, M., Koskela, M. M., & Mulo, P. (2017). Post-translational modifications in regulation of chloroplast function: recent advances. *Frontiers in plant science*, *8*, 240.

Guo, T., Chen, K., Dong, N. Q., Shi, C. L., Ye, W. W., Gao, J. P., ... & Lin, H. X. (2018). GRAIN SIZE AND NUMBER1 negatively regulates the OsMKKK10-OsMKK4-OsMPK6 cascade to coordinate the trade-off between grain number per panicle and grain size in rice. *The Plant Cell*, *30*(4), 871-888.

Hamel, L. P., Nicole, M. C., Sritubtim, S., Morency, M. J., Ellis, M., Ehlting, J., ... & Ellis, B. E. (2006). Ancient signals: comparative genomics of plant MAPK and MAPKK gene families. *Trends in plant science*, *11*(4), 192-198.

Hanks, S. K., Quinn, A. M., & Hunter, T. (1988). The protein kinase family: conserved features and deduced phylogeny of the catalytic domains. *Science*, *241*(4861), 42-52.

Hashimoto-Sugimoto, M., Negi, J., Monda, K., Higaki, T., Isogai, Y., Nakano, T., ... & Iba, K. (2016). Dominant and recessive mutations in the Raf-like kinase HT1 gene completely disrupt stomatal responses to CO2 in Arabidopsis. *Journal of Experimental Botany*, *67*(11), 3251-3261.

Hauser, T., Popilka, L., Hartl, F. U., & Hayer-Hartl, M. (2015). Role of auxiliary proteins in Rubisco biogenesis and function. *Nature Plants*, *1*(6), 1-11.

Hettenhausen, C., Baldwin, I. T., & Wu, J. (2012). Silencing MPK4 in Nicotiana attenuata enhances photosynthesis and seed production but compromises abscisic acid-induced stomatal closure and guard cell-mediated resistance to Pseudomonas syringae pv tomato DC3000. *Plant Physiology*, *158*(2), 759-776.

Hiyama, A., Takemiya, A., Munemasa, S., Okuma, E., Sugiyama, N., Tada, Y., ... & Shimazaki, K. I. (2017). Blue light and CO2 signals converge to regulate light-induced stomatal opening. *Nature communications*, *8*(1), 1284.

Houtz, R. L., Stults, J. T., Mulligan, R. M., & Tolbert, N. E. (1989). Post-translational modifications in the large subunit of ribulose bisphosphate carboxylase/oxygenase. *Proceedings of the National Academy of Sciences*, *86*(6), 1855-1859.

Jarvis, P., & López-Juez, E. (2013). Biogenesis and homeostasis of chloroplasts and other plastids. *Nature Reviews Molecular Cell Biology*, *14*(12), 787-802.

Jarvis, P., & Robinson, C. (2004). Mechanisms of protein import and routing in chloroplasts. *Current Biology*, *14*(24), R1064-R1077.

Jonwal, S., Verma, N., & Sinha, A. K. (2022). Regulation of photosynthetic light reaction proteins via reversible phosphorylation. *Plant Science*, *321*, 111312.

Jonwal, S., Rengasamy, B., & Sinha, A. K. (2023). Regulation of photosynthesis by mitogen-activated protein kinase in rice: antagonistic adjustment by OsMPK3 and OsMPK6. *Physiology and Molecular Biology of Plants*, *29*(9), 1247-1259.

Tõldsepp, K., Zhang, J., Takahashi, Y., Sindarovska, Y., Hõrak, H., Ceciliato, P. H., ... & Schroeder, J. I. (2018). Mitogen-activated protein kinases MPK 4 and MPK 12 are key components mediating CO 2-induced stomatal movements. *The Plant Journal*, *96*(5), 1018-1035.

Kalaji, H. M., Jajoo, A., Oukarroum, A., Brestic, M., Zivcak, M., Samborska, I. A., ... & Ladle, R. J. (2016). Chlorophyll a fluorescence as a tool to monitor physiological status of plants under abiotic stress conditions. *Acta physiologiae plantarum*, *38*(4), 102.

Kamps, M. P., & Sefton, B. M. (1986). Neither arginine nor histidine can carry out the function of lysine-295 in the ATP-binding site of p60src. *Molecular and cellular biology*, *6*(3), 751-757.

Kaul, R., Saluja, D., & Sachar, R. C. (1986). Phosphorylation of small subunit plays a crucial role in the regulation of RuBPCase in moss and spinach. *FEBS letters*, *209*(1), 63-70.

Lamberti, G., Gügel, I. L., Meurer, J., Soll, J., & Schwenkert, S. (2011). The cytosolic kinases STY8, STY17, and STY46 are involved in chloroplast differentiation in Arabidopsis. *Plant physiology*, *157*(1), 70-85.

Lee, D. W., Jung, C., & Hwang, I. (2013). Cytosolic events involved in chloroplast protein targeting. *Biochimica et Biophysica Acta (BBA)-Molecular Cell Research*, *1833*(2), 245-252.

Lee, D. W., Lee, S., Oh, Y. J., & Hwang, I. (2009). Multiple sequence motifs in the rubisco small subunit transit peptide independently contribute to Toc159-dependent import of proteins into chloroplasts. *Plant Physiology*, *151*(1), 129-141.

Lee, S., Lee, D. W., Lee, Y., Mayer, U., Stierhof, Y. D., Lee, S., ... & Hwang, I. (2009). Heat shock protein cognate 70-4 and an E3 ubiquitin ligase, CHIP, mediate plastid-destined precursor degradation through the ubiquitin-26S proteasome system in Arabidopsis. *The Plant Cell*, *21*(12), 3984-4001.

Li, Y., Gao, Y., Xu, X., Shen, Q., & Guo, S. (2009). Light-saturated photosynthetic rate in high-nitrogen rice (Oryza sativa L.) leaves is related to chloroplastic CO2 concentration. *Journal of Experimental Botany*, *60*(8), 2351-2360.

Li, N., Xu, R., & Li, Y. (2019). Molecular networks of seed size control in plants. *Annual review of plant biology*, *70*(1), 435-463.

Lin, M. T., Occhialini, A., Andralojc, P. J., Parry, M. A., & Hanson, M. R. (2014). A faster Rubisco with potential to increase photosynthesis in crops. *Nature*, *513*(7519), 547-550.

Liu, Z., Mei, E., Tian, X., He, M., Tang, J., Xu, M., ... & Bu, Q. (2021). OsMKKK70 regulates grain size and leaf angle in rice through the OsMKK4-OsMAPK6-OsWRKY53 signaling pathway. *Journal of integrative plant biology*, *63*(12), 2043-2057.

Long, S. P., & Bernacchi, C. J. (2003). Gas exchange measurements, what can they tell us about the underlying limitations to photosynthesis? Procedures and sources of error. *Journal of experimental botany*, *54*(392), 2393-2401.

Long, S. P., ZHU, X. G., Naidu, S. L., & Ort, D. R. (2006). Can improvement in photosynthesis increase crop yields?. *Plant, cell & environment*, *29*(3), 315-330.

Luo, X., Zheng, J., Huang, R., Huang, Y., Wang, H., Jiang, L., & Fang, X. (2016). Phytohormones signaling and crosstalk regulating leaf angle in rice. *Plant cell reports*, *35*(12), 2423-2433.

M. Hashimoto, J. Negi, J. Young, M. Israelsson, J. I. Schroeder, K. Iba, *Arabidopsis* HT1 kinase controls stomatal movements in response to CO_2. *Nat. Cell Biol.***8**,391–397 (2006).

Manna, M., Rengasamy, B., & Sinha, A. K. (2023). Revisiting the role of MAPK signalling pathway in plants and its manipulation for crop improvement. *Plant, Cell & Environment*, *46*(8), 2277-2295.

Ma, H., Li, J., Ma, L., Wang, P., Xue, Y., Yin, P., ... & Wang, S. (2021). Pathogen-inducible OsMPKK10. 2-OsMPK6 cascade phosphorylates the Raf-like kinase OsEDR1 and inhibits its scaffold function to promote rice disease resistance. *Molecular plant*, *14*(4), 620-632.

Mathan, J., Bhattacharya, J., & Ranjan, A. (2016). Enhancing crop yield by optimizing plant developmental features. *Development*, *143*(18), 3283-3294.

May, T., & Soll, J. (2000). 14-3-3 proteins form a guidance complex with chloroplast precursor proteins in plants. *The Plant Cell*, *12*(1), 53-63.

Murchie, E. H., & Lawson, T. (2013). Chlorophyll fluorescence analysis: a guide to good practice and understanding some new applications. *Journal of experimental botany*, *64*(13), 3983-3998.

Murchie, E. H., & Niyogi, K. K. (2011). Manipulation of photoprotection to improve plant photosynthesis. *Plant physiology*, *155*(1), 86-92.

Nakagami, H., Kiegerl, S., & Hirt, H. (2004). OMTK1, a novel MAPKKK, channels oxidative stress signaling through direct MAPK interaction. *Journal of Biological Chemistry*, *279*(26), 26959-26966.

Ning, J., Zhang, B., Wang, N., Zhou, Y., & Xiong, L. (2011). Increased leaf angle1, a Raf-like MAPKKK that interacts with a nuclear protein family, regulates mechanical tissue formation in the Lamina joint of rice. *The Plant Cell*, *23*(12), 4334-4347.

Nolan, T. M., Vukašinović, N., Liu, D., Russinova, E., & Yin, Y. (2020). Brassinosteroids: multidimensional regulators of plant growth, development, and stress responses. *The plant cell*, *32*(2), 295-318.

Ort, D. R., Merchant, S. S., Alric, J., Barkan, A., Blankenship, R. E., Bock, R., ... & Zhu, X. G. (2015). Redesigning photosynthesis to sustainably meet global food and bioenergy demand. *Proceedings of the national academy of sciences*, *112*(28), 8529-8536.

Parry, M. A. J., Madgwick, P. J., Carvalho, J. F. C., & Andralojc, P. J. (2007). Prospects for increasing photosynthesis by overcoming the limitations of Rubisco. *The Journal of Agricultural Science*, *145*(1), 31.

Parry, M. A., Andralojc, P. J., Scales, J. C., Salvucci, M. E., Carmo-Silva, A. E., Alonso, H., & E, S. M. (2013). Rubisco activity and regulation as targets for crop improvement. *Journal of experimental botany*, *64*(3), 717-730.

Porra, R. J., Thompson, W. A., & Kriedemann, P. E. (1989). Determination of accurate extinction coefficients and simultaneous equations for assaying chlorophylls a and b extracted with four different solvents: verification of the concentration of chlorophyll standards by atomic absorption spectroscopy. *Biochimica et Biophysica Acta (BBA)-Bioenergetics*, *975*(3), 384-394.

Puthiyaveetil, S., & Allen, J. F. (2009). Chloroplast two-component systems: evolution of the link between photosynthesis and gene expression. *Proceedings of the Royal Society B: Biological Sciences*, *276*(1665), 2133-2145.

Puthiyaveetil, S., Ibrahim, I. M., Jeličić, B., Tomašić, A., Fulgosi, H., & Allen, J. F. (2010). Transcriptional control of photosynthesis genes: the evolutionarily conserved regulatory mechanism in plastid genome function. *Genome biology and evolution*, *2*, 888-896.

Raghuram, B., Sheikh, A. H., Rustagi, Y., & Sinha, A. K. (2015). Micro RNA biogenesis factor DRB 1 is a phosphorylation target of mitogen activated protein kinase MPK 3 in both rice and Arabidopsis. *The FEBS journal*, *282*(3), 521-536.

Rao, K. P., Richa, T. A. M. B. I., Kumar, K. U. N. D. A. N., Raghuram, B. A. D. M. I., & Sinha, A. K. (2010). In silico analysis reveals 75 members of mitogen-activated protein kinase kinase kinase gene family in rice. *DNA research*, *17*(3), 139-153.

Reiland, S., Finazzi, G., Endler, A., Willig, A., Baerenfaller, K., Grossmann, J., ... & Baginsky, S. (2011). Comparative phosphoproteome profiling reveals a function of the STN8 kinase in fine-tuning of cyclic electron flow (CEF). *Proceedings of the National Academy of Sciences*, *108*(31), 12955-12960.

Reiland, S., Messerli, G., Baerenfaller, K., Gerrits, B., Endler, A., Grossmann, J., ... & Baginsky, S. (2009). Large-scale Arabidopsis phosphoproteome profiling reveals novel chloroplast kinase substrates and phosphorylation networks. *Plant physiology*, *150*(2), 889-903.

Rengasamy, B., Manna, M., Jonwal, S., Sathiyabama, M., Thajuddin, N. B., & Sinha, A. K. (2024). A simplified and improved protocol of rice transformation to cater wide range of rice cultivars. *Protoplasma*, *261*(4), 641-654.

Rochaix, J. D. (2014). Regulation and dynamics of the light-harvesting system. *Annual review of plant biology*, *65*, 287-309.

Rodriguez, M. C., Petersen, M., & Mundy, J. (2010). Mitogen-activated protein kinase signaling in plants. *Annual Review of Plant Biology, 61*, 621-649.

Rudrabhatla, P., Reddy, M. M., & Rajasekharan, R. (2006). Genome-wide analysis and experimentation of plant serine/threonine/tyrosine-specific protein kinases. *Plant Molecular Biology*, *60*(2), 293-319.

Schönberg, A., & Baginsky, S. (2012). Signal integration by chloroplast phosphorylation networks: an update. *Frontiers in plant science*, *3*, 256.

Schönberg, A., Rödiger, A., Mehwald, W., Galonska, J., Christ, G., Helm, S., ... & Baginsky, S. (2017). Identification of STN7/STN8 kinase targets reveals connections between electron transport, metabolism and gene expression. *The Plant Journal*, *90*(6), 1176-1186.

Sharkey, T. D. (1985). Photosynthesis in intact leaves of C3 plants: physics, physiology and rate limitations. *The Botanical Review*, *51*(1), 53-105.

Sharkey, T. D. (2015). What gas exchange data can tell us about photosynthesis. *Plant, cell & environment*, *39*(6), 1161-1163.

Sharkey, T. D., Bernacchi, C. J., Farquhar, G. D., & Singsaas, E. L. (2007). Fitting photosynthetic carbon dioxide response curves for C3 leaves. *Plant, cell & environment*, *30*(9), 1035-1040.

Sharma, A., Kumar, V., Shahzad, B., Ramakrishnan, M., Singh Sidhu, G. P., Bali, A. S., ... & Zheng, B. (2020). Photosynthetic response of plants under different abiotic stresses: a review. *Journal of Plant Growth Regulation*, *39*(2), 509-531.

Sharwood, R. E. (2017). Engineering chloroplasts to improve Rubisco catalysis: prospects for translating improvements into food and fiber crops. *New Phytologist*, *213*(2), 494-510.

Shen, J., Fu, J., Ma, J., Wang, X., Gao, C., Zhuang, C., ... & Jiang, L. (2014). Isolation, culture, and transient transformation of plant protoplasts. *Current protocols in cell biology*, *63*(1), 2-8.

Shilpha, J., Song, J., & Jeong, B. R. (2023). Ammonium phytotoxicity and tolerance: An insight into ammonium nutrition to improve crop productivity. *Agronomy*, *13*(6), 1487.

Simkin, A. J., López-Calcagno, P. E., & Raines, C. A. (2019). Feeding the world: improving photosynthetic efficiency for sustainable crop production. *Journal of Experimental Botany*, *70*(4), 1119-1140.

Singh, P., Ara, H., Tayyeba, S., Pandey, C., & Sinha, A. K. (2019). Development of efficient protocol for rice transformation overexpressing MAP kinase and their effect on root phenotypic traits. *Protoplasma*, *256*(4), 997-1011.

Sinha, A. K., Jaggi, M., Raghuram, B., & Tuteja, N. (2011). Mitogen-activated protein kinase signaling in plants under abiotic stress. *Plant signaling & behavior*, *6*(2), 196-203.

Snyder, M. A., Bishop, J. M., McGrath, J. P., & Levinson, A. D. (1985). A mutation at the ATP-binding site of pp60v-src abolishes kinase activity, transformation, and tumorigenicity. *Molecular and cellular biology*, *5*(7), 1772-1779.

Spreitzer, R. J. (2003). Role of the small subunit in ribulose-1, 5-bisphosphate carboxylase/oxygenase. *Archives of biochemistry and biophysics*, *414*(2), 141-149.

Su J, Yang L, Zhu Q, Wu H, He Y, Liu Y et al (2018). Active photosynthetic inhibition mediated by MPK3/MPK6 is critical to effector-triggered immunity. *PLoS biology*, *16*(5), e2004122.

Suzuki, Y., Ohkubo, M., Hatakeyama, H., Ohashi, K., Yoshizawa, R., Kojima, S., ... & Makino, A. (2007). Increased Rubisco content in transgenic rice transformed with the 'sense'rbcS gene.

Takahashi, Y., Bosmans, K.C., Hsu, P.K., Paul, K., Seitz, C., Yeh, C.Y., Wang, Y.S., Yarmolinsky, D., Sierla, M., Vahisalu, T. and Waszczak, C., (2022). Stomatal CO2/bicarbonate sensor consists of two interacting protein kinases, Raf-like HT1 and non-kinase-activity requiring MPK12/MPK4. *Science Advances*, *8*(49), p.eabq6161.

Terashima, I., Hanba, Y. T., Tholen, D., & Niinemets, Ü. (2011). Leaf functional anatomy in relation to photosynthesis. *Plant physiology*, *155*(1), 108-116.

Tikkanen, M., & Aro, E. M. (2012). Thylakoid protein phosphorylation in dynamic regulation of photosystem II in higher plants. *Biochimica et Biophysica Acta (BBA)-Bioenergetics*, *1817*(1), 232-238.

Von Caemmerer, S. (2000). *Biochemical models of leaf photosynthesis*. Csiro publishing.

Waegemann, K., & Soll, J. (1996). Phosphorylation of the transit sequence of chloroplast precursor proteins. *Journal of Biological Chemistry*, *271*(11), 6545-6554.

Witoń, D., Gawroński, P., Czarnocka, W., Ślesak, I., Rusaczonek, A., Sujkowska-Rybkowska, M., ... & Karpiński, S. (2016). Mitogen activated protein kinase 4 (MPK4) influences growth in Populus tremula L.× tremuloides. *Environmental and Experimental Botany*, *130*, 189-205.

Witoń, D., Sujkowska-Rybkowska, M., Dąbrowska-Bronk, J., Czarnocka, W., Bernacki, M., Szechyńska-Hebda, M., & Karpiński, S. (2021). MITOGEN-ACTIVATED PROTEIN KINASE 4 impacts leaf development, temperature, and stomatal movement in hybrid aspen. *Plant Physiology*, *186*(4), 2190-2204.

Wu, A., Hammer, G. L., Doherty, A., von Caemmerer, S., & Farquhar, G. D. (2019). Quantifying impacts of enhancing photosynthesis on crop yield. *Nature plants*, *5*(4), 380-388.

Xiong, D. (2024). Perspectives of improving rice photosynthesis for higher grain yield. *Crop and Environment*, *3*(3), 123-137.

Zhang, Y., Su, J., Duan, S., Ao, Y., Dai, J., Liu, J., ... & Wang, H. (2011). A highly efficient rice green tissue protoplast system for transient gene expression and studying light/chloroplast-related processes. *Plant methods*, *7*(1), 30.

Zhu, X. G., Long, S. P., & Ort, D. R. (2010). Improving photosynthetic efficiency for greater yield. *Annual review of plant biology*, *61*(1), 235-261.

Zhu, X., Zhang, N., Liu, X., Li, S., Yang, J., Hong, X., ... & Si, H. (2021). Mitogen-activated protein kinase 11 (MAPK11) maintains growth and photosynthesis of potato plant under drought condition. *Plant Cell Reports*, *40*, 491-506.

Zhu, X., Zhang, N., Liu, X., Wang, S., Li, S., Yang, J., ... & Si, H. (2020). StMAPK3 controls oxidase activity, photosynthesis and stomatal aperture under salinity and osmosis stress in potato. *Plant Physiology and Biochemistry*, *156*, 167-177.

1184 **Tables with legends:**

1185 **Table 1: CO_2-saturated maximum photosynthesis (A_{max}), maximum *in vivo* Rubisco activity**
1186 **(V_{cmax}), maximum electron transport rate (J), and maximum rate of triose phosphate**
1187 **utilization (*TPU*) of WT, *MPK3 OE* and *mpk3 ko* lines through A/C_i curve analysis.**

	Amean	*Amax*	*Vcmax*	*J*	*TPU*
WT	25.17 ± 2.34	36.18 ± 1.37	110.2 ± 5.58	142.4 ± 8.23	9.28 ± 0.38
MPK3-23 MOCK	25.48 ± 1.8	35.16 ± 1.6	88.29 ± 6.348	133.16 ± 5.75	8.73 ± 0.45
MPK3-23 DEX	17.75 ± 2.34	26.53 ± 3.2	61.77 ± 9.32	101.89 ± 11.5	6.94 ± 0.688
MPK3-24 MOCK	24.02 ± 3.10	34.22 ± 0.87	88.368 ± 9.23	132.72 ± 7.9	8.73 ± .078
MPK3-24 DEX	17.67 ± 1.43	28.57 ± 0.51	68.79 ± 10.83	116.92 ± 4.18	7.6 ± 0.17
mpk3 ko1	29.78 ± 1.75	40.83 ± 1.41	126.3 ± 3.2	165.12 ± 6.58	10.66 ± 0.4
mpk3 ko2	30.48 ± 1.28	41.8 ± 0.4	126.56 ± 2.54	163.65 ± 1.9	10.66 ± 0.02

1188 **Table 2: CO_2-saturated maximum photosynthesis (A_{max}), maximum *in vivo* Rubisco activity**
1189 **(V_{cmax}), maximum electron transport rate (J), and maximum rate of triose phosphate**
1190 **utilization (*TPU*) of WT, *ACTPK1 OE* and *actpk1 ko* lines through A/C_i curve analysis.**

	Amean	*Amax*	*Vcmax*	*J*	*TPU*
WT	22.27 ± 1.12	38.8 ± 1.08	88.18 ± 3.14	130.36 ± 7.36	9.5 ± 0.31
ACTPK1 OE19	21.89 ± 0.55	41.34 ± 0.37	88.25 ± 2.48	124.79 ± 6.37	9.13 ± 0.61
ACTPK1 OE24	18.42 ± 1.17	39.98 ± 0.26	105.77 ± 1.29	141.49 ± 4.39	10.28 ± 0.12
ACTPK1 OE33	19.08 ± 0.56	37.5 ± 1.36	95.05 ± 3.88	133.93 ± 12.95	10.3 ± 0.96
actpk1 ko12	12.22 ± 0.42	25.65 ± 0.44	67.6 ± 8.85	72.58 ± 9.65	6.53 ± 0.23
actpk1 ko14	14.10 ± 2.03	26.03 ± 0.54	59.89 ± 4.42	65.23 ± 5.89	6.42 ± 0.65
actpk1 ko19	12.59 ± 1.93	26.48 ± 0.7	62.38 ± 6.36	73.32 ± 9.63	5.98 ± 1.19

1191

1192

Figures with legends:

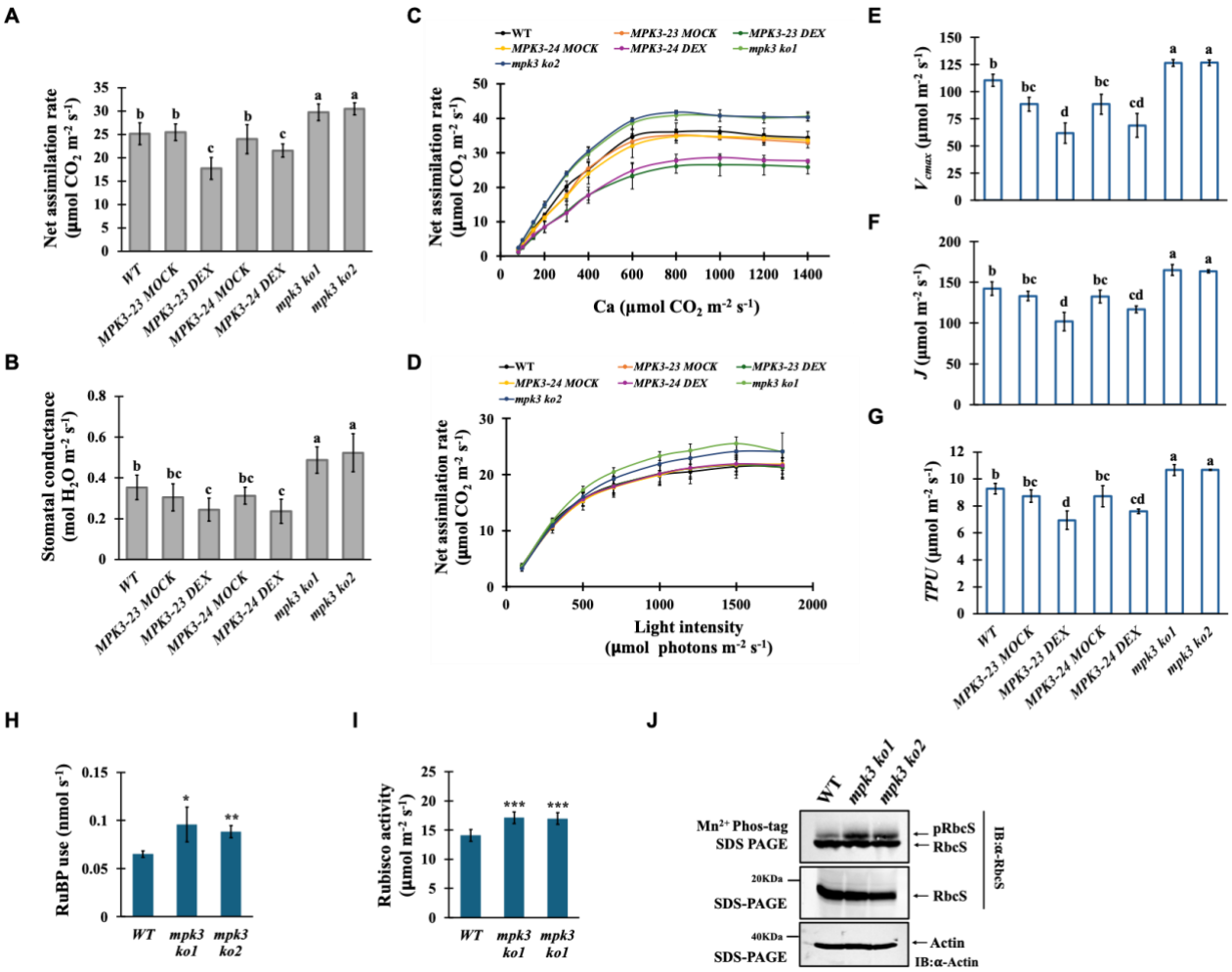

Fig. 1. MPK3 negatively regulates photosynthesis. **A)** Bar graph showing net assimilation rate in WT, *MPK3 OE* (*MPK3-23*, *MPK3-24*) and *mpk3 ko* (*mpk3 ko1*, *mpk3 ko2*) plants at ambient CO_2 (400 µmol mol^{-1}). **B)** Bar graph showing Stomatal conductance to water in WT, *MPK3 OE* (*MPK3-23*, *MPK3-24*) and *mpk3 ko* (*mpk3 ko1*, *mpk3 ko2*) plants at ambient CO_2 (400 µmol mol^{-1}). **C)** Quantification of net photosynthesis per unit area of WT, *MPK3 OE* (*MPK3-23*, *MPK3-24*) and *mpk3 ko* (*mpk3 ko1*, *mpk3 ko2*) plants in response to varying CO_2 concentration at 1500 µmol m^{-2} s^{-1} light intensity (*A/Ci* curve). Each value represents mean ± SD, where n = at least three data points from different plants. **D)** Quantification of net photosynthesis per unit area of WT, *MPK3 OE* (*MPK3-23*, *MPK3-24*) and *mpk3 ko* (*mpk3 ko1*, *mpk3 ko2*) plants in response to increasing PPFD at 400 µmol mol^{-1} CO_2 concentration (*A/Q* curve). Each value represents mean ± SD, where n = at least three data points from different plants. **E)** Bar graph showing maximum rate of carboxylation (*Vcmax*) in WT, *MPK3 OE* (*MPK3-23*, *MPK3-24*) and *mpk3 ko* (*mpk3 ko1*, *mpk3 ko2*) plants. **F)** Bar graph showing electron transport rate (*J*) in WT, *MPK3 OE* (*MPK3-23*, *MPK3-24*) and *mpk3 ko* (*mpk3 ko1*, *mpk3 ko2*) plants. **G)** Bar graph showing triose phosphate utilisation (*TPU*) in WT, *MPK3 OE* (*MPK3-23*, *MPK3-24*) and *mpk3 ko* (*mpk3 ko1*, *mpk3 ko2*) plants. Data represented in D), E) and F) are deduced by fitting *A/Ci* curve using FvcB model. MOCK, dimethyl sulfoxide treated (DMSO) plants; DEX, dexamethasone treated plants. 1 µM DMSO and DEX sprayed on *MPK3 OE* leaves, 24 h prior to taking measurements. All the measurements were taken from flag leaf at heading stage using LiCOR6800, between 8:00 am to 11:00 am. Different letters indicate statistical significance according to one-way ANOVA followed by post-hoc Tukey HSD calculation at $P < 0.05$. **H)** Bar graph showing RuBP use in WT, *MPK3 OE* (*MPK3-23*, *MPK3-24*) and *mpk3 ko* (*mpk3 ko1*, *mpk3 ko2*) plants. **I)** Bar graph showing Rubisco activity in WT, *MPK3 OE* (*MPK3-23*, *MPK3-24*) and *mpk3 ko* (*mpk3 ko1*, *mpk3 ko2*) plants**.** Values represent the

1217 mean ± SD (*n* = 3 biological replicates). Asterix indicate statistical significance according to student
1218 ttest (*P*<0.05). **J)** Phos-tag gel western blots showing phosphorylated and non-phosphorylated RbcS
1219 content in WT and *mpk3 ko* lines. Blots were developed by α-RbcS antibody. Actin was used as
1220 endogenous control.

1221

1222

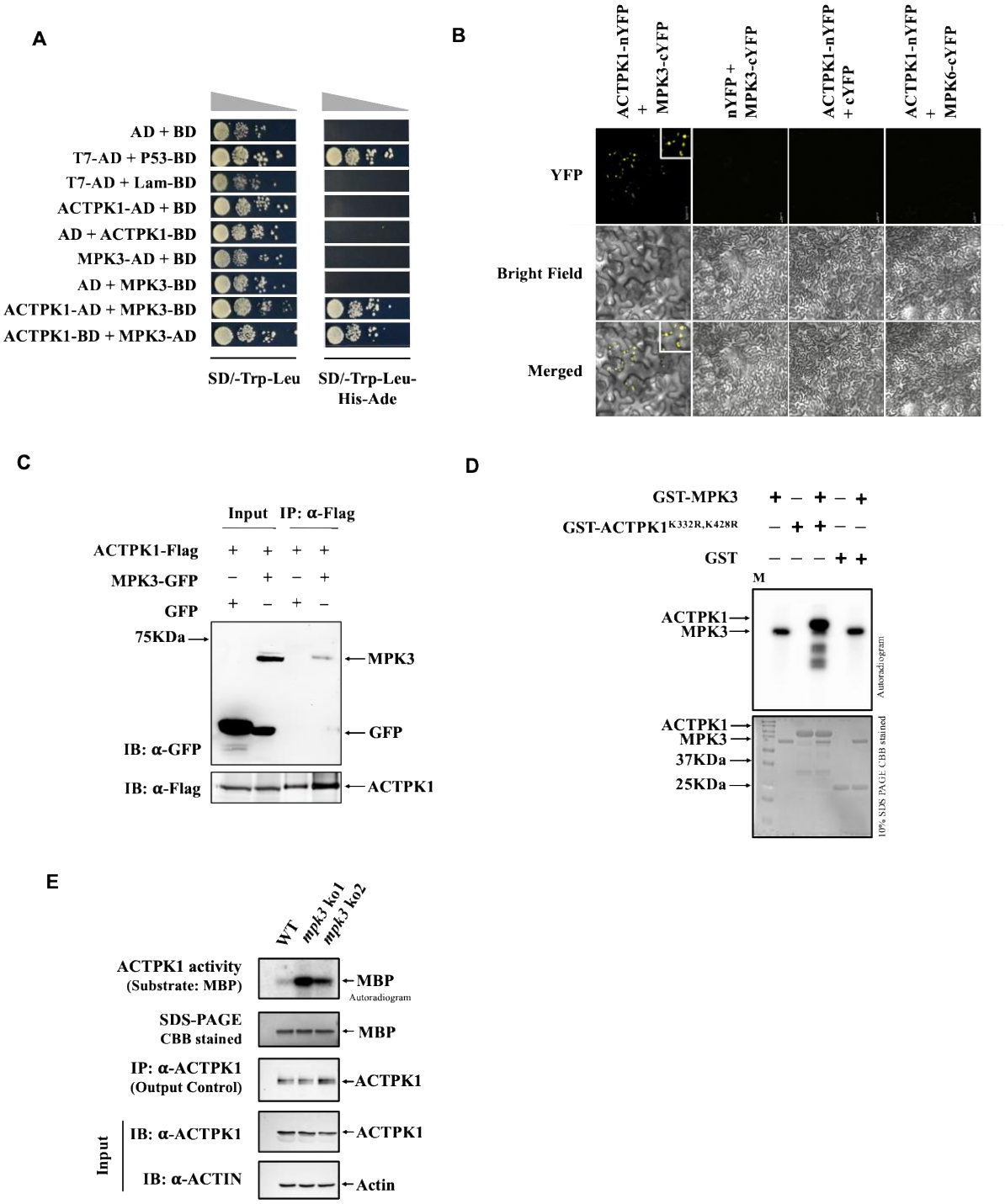

1223

1224 **Fig. 2. MPK3 physically interacts with and phosphorylates ACTPK1 to inhibit its activity. A)** MPK3
1225 interacts with ACTPK1 in yeast cells. Yeast cells were cultured on SD/-Trp-Leu and SD/-Trp-Leu-His-
1226 Ade media. AD, GAL4 activation domain; BD, GAL4 DNA-binding domain; SD, synthetic defined. **B)** BiFC
1227 assays showing that MPK3 interacts with ACTPK1 in *N. benthamiana*. ACTPK1-nYFP was co-
1228 transformed with MPK3-cYFP in fully expanded leaves of *N. benthamiana*. The ACTPK1-nYFP/MPK6-
1229 cYFP and Empty-nYFP/MPK3-cYFP were used as negative controls. Inset on top right is the enlarged
1230 image of signal. Scale Bar, 25 μm. **C)** Interaction between MPK3 and ACTPK1 in the Co-IP assays. α-
1231 Flag beads were used to immunoprecipitate ACTPK1 protein. Gel blots were probed with α-GFP
1232 antibody. **D)** *In vitro* kinase assay showing phosphorylation of kinase dead GST-ACTPK1^{K332R,K428R} by

1233 GST-MPK3. CBB (Coomassie Brilliant Blue) stained 10% SDS page gel shows loaded proteins. **E)** IP-
1234 Kinase showing ACTPK1 immunoprecipitated from *mpk3 ko* enhances MBP phosphorylation. ACTPK1
1235 was immunoprecipitated using α-ACTPK1 antibody.

1236

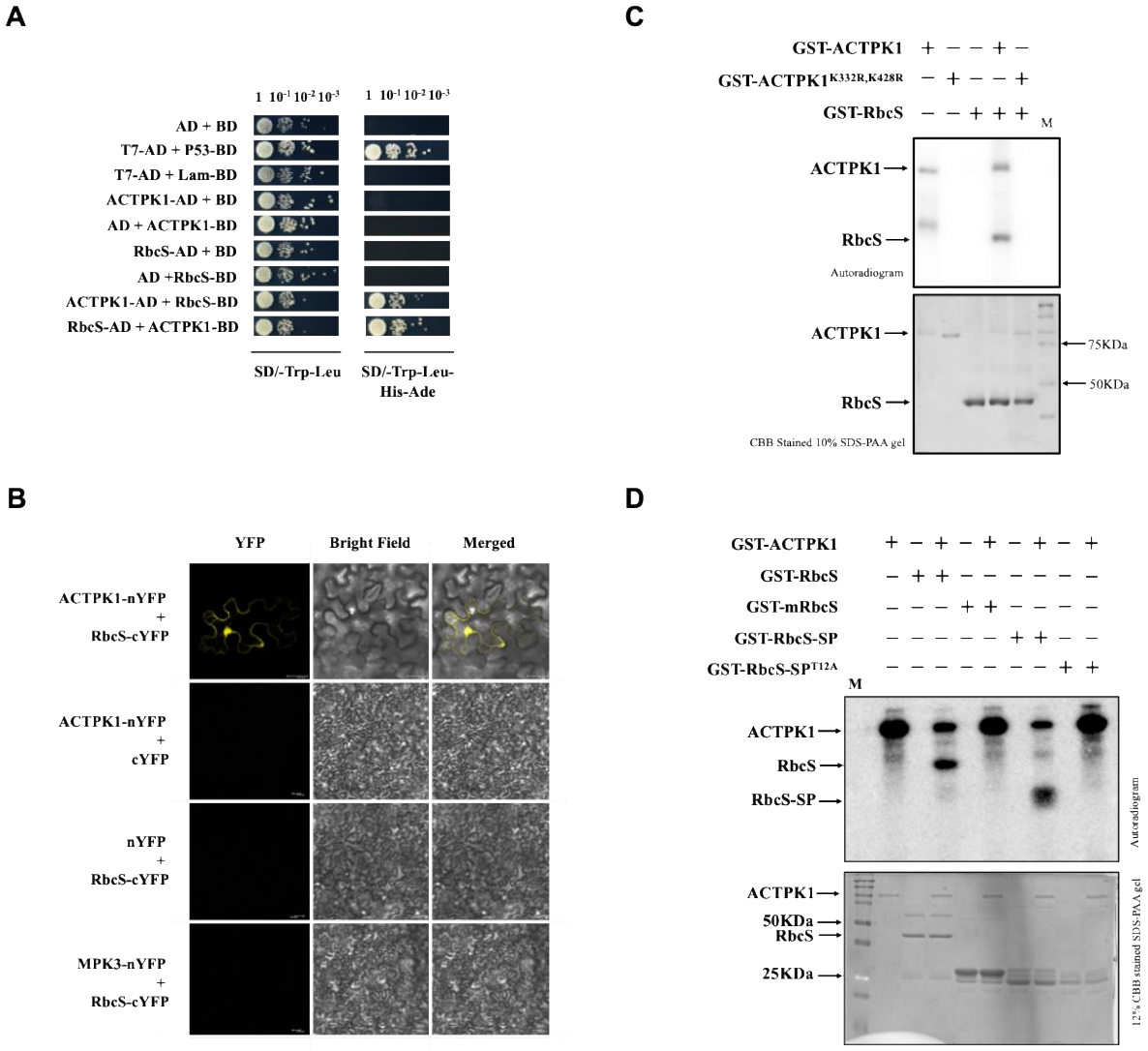

Fig. 3. ACTPK1 physically interacts with and phosphorylates RbcS within signal peptide. A) ACTPK1 interacts with RbcS in yeast cells. Yeast cells were cultured on SD/-Trp-Leu and SD/-Trp-Leu-His-Ade media. AD, GAL4 activation domain; BD, GAL4 DNA-binding domain; SD, synthetic defined. **B)** BiFC assays showing that ACTPK1 interacts with RbcS in *N. benthamiana* mesophyll cell. ACTPK1-nYFP was co-transformed with RbcS-cYFP in fully expanded leaves of *N. benthamiana*. The ACTPK1-nYFP/cYFP, nYFP/RbcS-cYFP and MPK3-nYFP/RbcS-cYFP were used as negative controls. Scale Bar, 25 µm. **C)** *In vitro* kinase assay showing phosphorylation of kinase dead GST-RbcS by GST-ACTPK1. CBB stained 10% SDS PAA gel shows loaded proteins. **D)** *In vitro* kinase assay showing ACTPK1 specifically phosphorylates Thr12 residue of RbcS**.** CBB stained 12% SDS PAA gel shows loaded proteins.

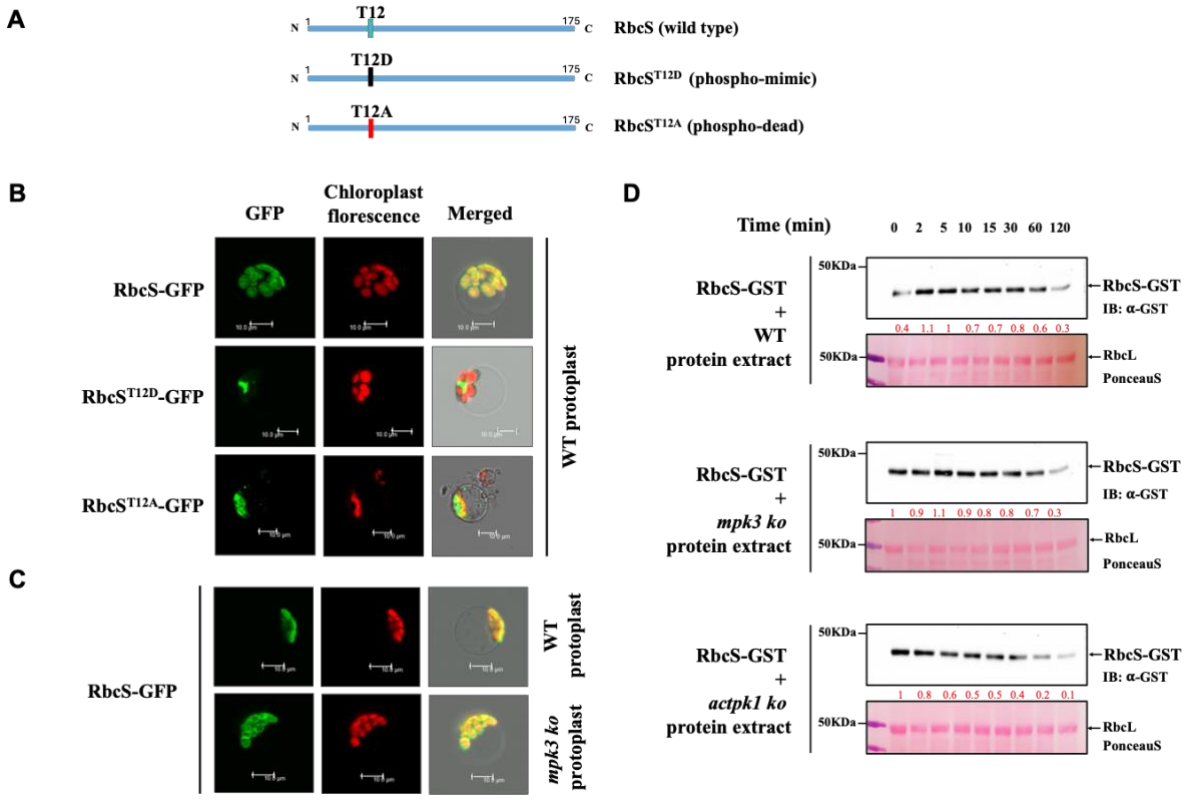

Fig. 4. ACTPK1 regulates stability and import of RbcS into the chloroplast. A) Pictorial representation of RbcS, RbcS^{T12D} (phosphor-mimic), RbcS^{T12A} (phosphor-dead) mutant constructs designed through site-directed mutagenesis. **B)** Localization of RbcS, RbcS^{T12D}, RbcS^{T12A} in protoplast isolated from WT rice seedlings. Scale Bar, 10 µm. **C)** Localization of RbcS in protoplast isolated from WT and *mpk3 ko* rice seedlings. Scale Bar, 10 µm **D)** Western blots of cell-free degradation assays showing degradation of GST-RbcS when incubated with crude extract of WT (upper panel), *mpk3 ko* (middle panel) and *actpk1 ko* (lower panel). Ponceau stained (PonceauS) blot shows RbcL protein. Band intensities are mentioned with red colour. Band intensities were quantified using ImageJ software.

1260

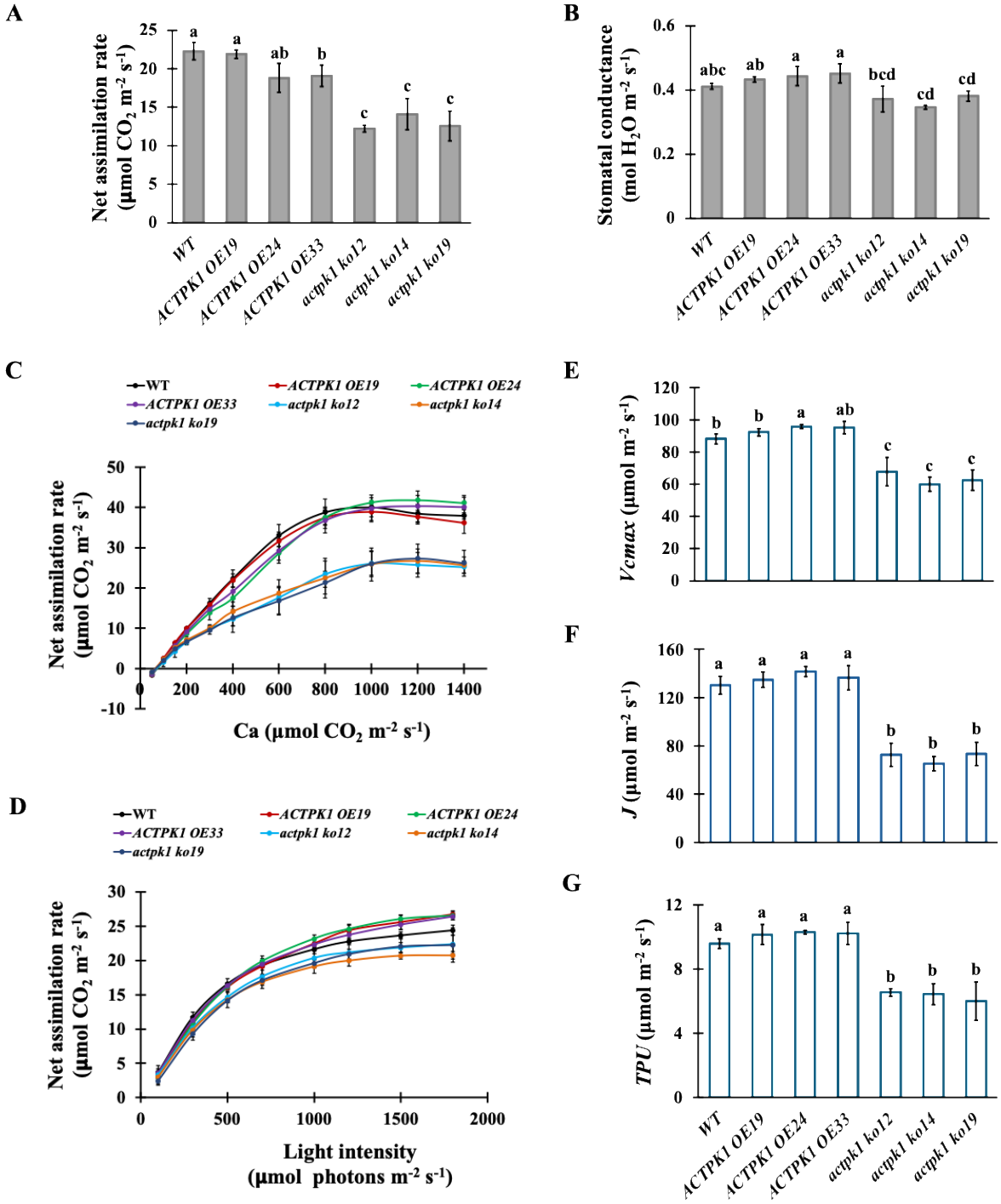

1261

1262 **Fig. 5. ACTPK1 positively regulates photosynthesis in rice. A)** Bar graph showing net assimilation rate
1263 in WT, *ACTPK1 OE* (*ACTPK1 OE19, ACTPK1 OE24 & ACTPK1 OE33*) and *actpk1 ko* (*actpk1 ko12, actpk1*
1264 *ko14 & actpk1 ko19*) plants at ambient CO_2 (400 µmol mol^{-1}). **B)** Bar graph showing Stomatal
1265 conductance to water in WT, *ACTPK1 OE* (*ACTPK1 OE19, ACTPK1 OE24 & ACTPK1 OE33*) and *actpk1 ko*
1266 (*actpk1 ko12, actpk1 ko14 & actpk1 ko19*) plants at ambient CO_2 (400 µmol mol^{-1}). **C)** Quantification
1267 of net photosynthesis per unit area of WT, *ACTPK1 OE* (*ACTPK1 OE19, ACTPK1 OE24 & ACTPK1 OE33*)
1268 and *actpk1 ko* (*actpk1 ko12, actpk1 ko14 & actpk1 ko19*) plants in response to varying CO_2
1269 concentration at 1500 µmol m^{-2} s^{-1} light intensity (*A/Ci* curve). Each value represents mean ± SD (n =
1270 at least three biological replicate). **D)** Quantification of net photosynthesis per unit area of WT, *ACTPK1*

1271 *OE* (*ACTPK1 OE19, ACTPK1 OE24 & ACTPK1 OE33*) and *actpk1 ko* (*actpk1 ko12, actpk1 ko14 & actpk1*
1272 *ko19*) plants in response to increasing PPFD at 400 µmol mol^{-1} CO_2 concentration (*A/Q* curve). Each
1273 value represents mean ± SD (n = at least three biological replicate). **E)** Bar graph showing maximum
1274 rate of carboxylation (*Vcmax*) in WT, *ACTPK1 OE* (*ACTPK1 OE19, ACTPK1 OE24 & ACTPK1 OE33*) and
1275 *actpk1 ko* (*actpk1 ko12, actpk1 ko14 & actpk1 ko19*) plants. **F)** Bar graph showing electron transport
1276 rate (*J*) in WT, *ACTPK1 OE* (*ACTPK1 OE19, ACTPK1 OE24 & ACTPK1 OE33*) and *actpk1 ko* (*actpk1 ko12,*
1277 *actpk1 ko14 & actpk1 ko19*) plants. **G)** Bar graph showing triose phosphate utilisation (*TPU*) in WT,
1278 *ACTPK1 OE* (*ACTPK1 OE19, ACTPK1 OE24 & ACTPK1 OE33*) and *actpk1 ko* (*actpk1 ko12, actpk1 ko14 &*
1279 *actpk1 ko19*) plants. Data represented in E), F) and G) are deduced by fitting *A/Ci* curve using FvcB
1280 model. All the measurements were taken from flag leaf at heading stage using LiCOR6800, between
1281 8:00 am to 11:00 am. Different letters indicate statistical significance according to one-way ANOVA
1282 followed by post-hoc Tukey HSD calculation at $P < 0.05$.

1283

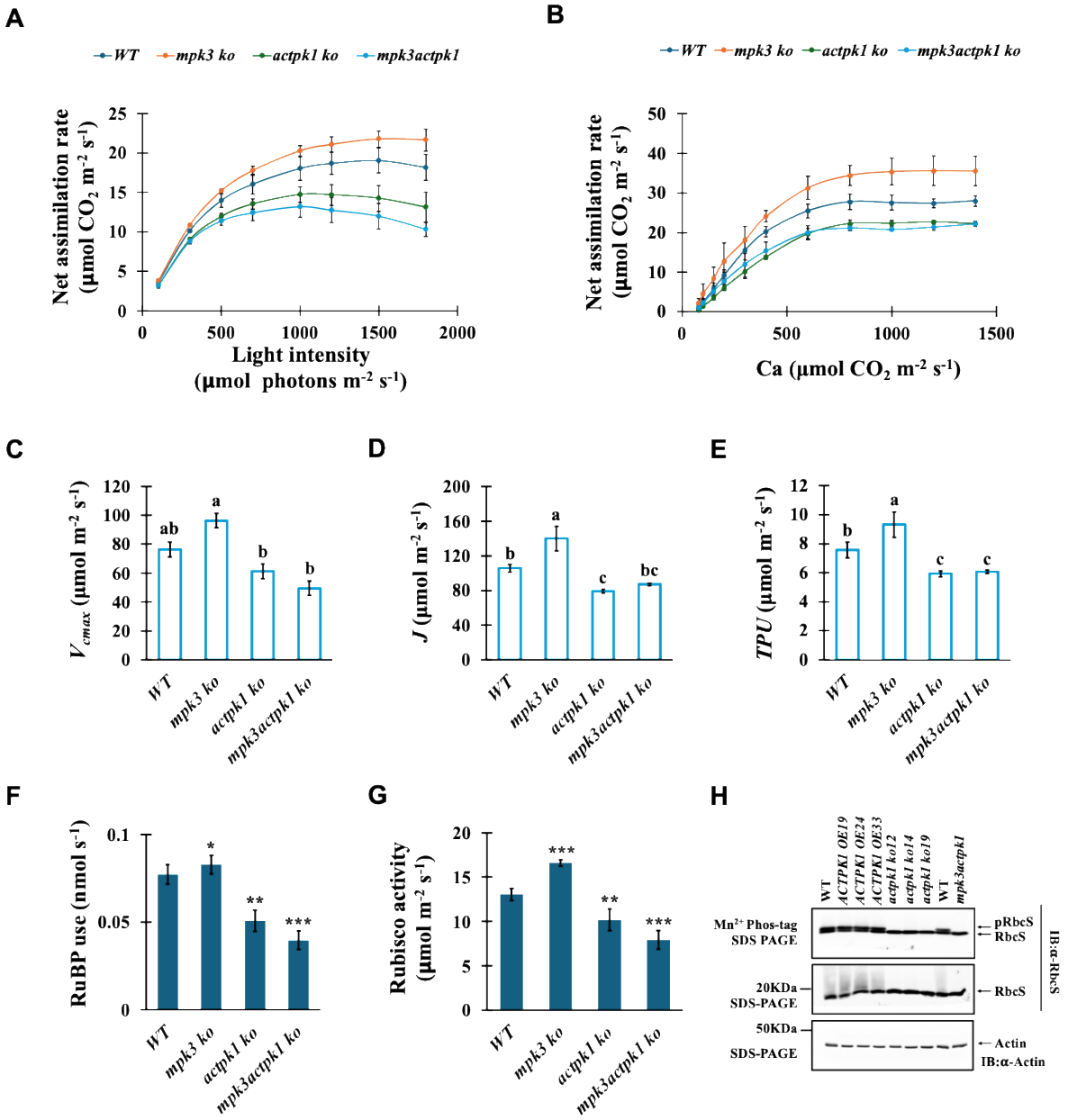

Fig. 6. ACTPK1 acts downstream of MPK3 to regulates photosynthesis in rice. A) Comparison of net photosynthesis per unit area of WT, *mpk3 ko*, *actpk1 ko* and *mpk3actpk1 ko* plants in response to varying CO_2 concentration at 1500 µmol m^{-2} s^{-1} light intensity (*A/Ci* curve). Each value represents mean ± SD, where n = at least three data points from different plants. **B)** Comparison of net photosynthesis per unit area of WT, *mpk3 ko*, *actpk1 ko* and *mpk3actpk1 ko* plants in response to increasing PPFD at 400 µmol mol^{-1} CO_2 concentration (*A/Q* curve). Each value represents mean ± SD, where n = at least three data points from different plants. **C)** Bar graph showing electron transport rate (*J*) in of WT, *mpk3 ko*, *actpk1 ko* and *mpk3actpk1 ko* plants. **D)** Bar graph showing maximum rate of carboxylation (*Vcmax*) in of WT, *mpk3 ko*, *actpk1 ko* and *mpk3actpk1 ko* plants. **E)** Bar graph showing triose phosphate utilisation (*TPU*) in of WT, *mpk3 ko*, *actpk1 ko* and *mpk3actpk1 ko* plants. Data represented in D), E) and F) are deduced by fitting *A/Ci* curve using FvcB model. All the measurements were taken from flag leaf at heading stage using LiCOR6800, between 8:00 am to 11:00 am. Different letters indicate statistical significance according to one-way ANOVA followed by post-hoc Tukey HSD calculation at $P < 0.05$. **F)** Bar graph showing RuBP use in in WT, *ACTPK1 OE* (*ACTPK1 OE19, ACTPK1*

1300 *OE24 & ACTPK1 OE33*) and *actpk1 ko* (*actpk1 ko12, actpk1 ko14 & actpk1 ko19*)and *mpk3actpk1 ko*
1301 lines. **G)** Bar graph showing Rubisco activity in WT, *ACTPK1 OE* (*ACTPK1 OE19, ACTPK1 OE24 & ACTPK1*
1302 *OE33*) and *actpk1 ko* (*actpk1 ko12, actpk1 ko14 & actpk1 ko19*)and *mpk3actpk1 ko* lines. Values
1303 represent the mean ± SD (*n* = 3 biological replicates). Asterix indicate statistical significance according
1304 to student ttest (*P*<0.05). **H)** Phos-tag gel western blots showing phosphorylated and non-
1305 phosphorylated RbcS content in WT, *ACTPK1 OE* (*ACTPK1 OE19, ACTPK1 OE24 & ACTPK1 OE33*) and
1306 *actpk1 ko* (*actpk1 ko12, actpk1 ko14 & actpk1 ko19*)and *mpk3actpk1 ko* (double mutant) lines. Blots
1307 were developed by α-RbcS antibody. Actin was used as endogenous control.

1308

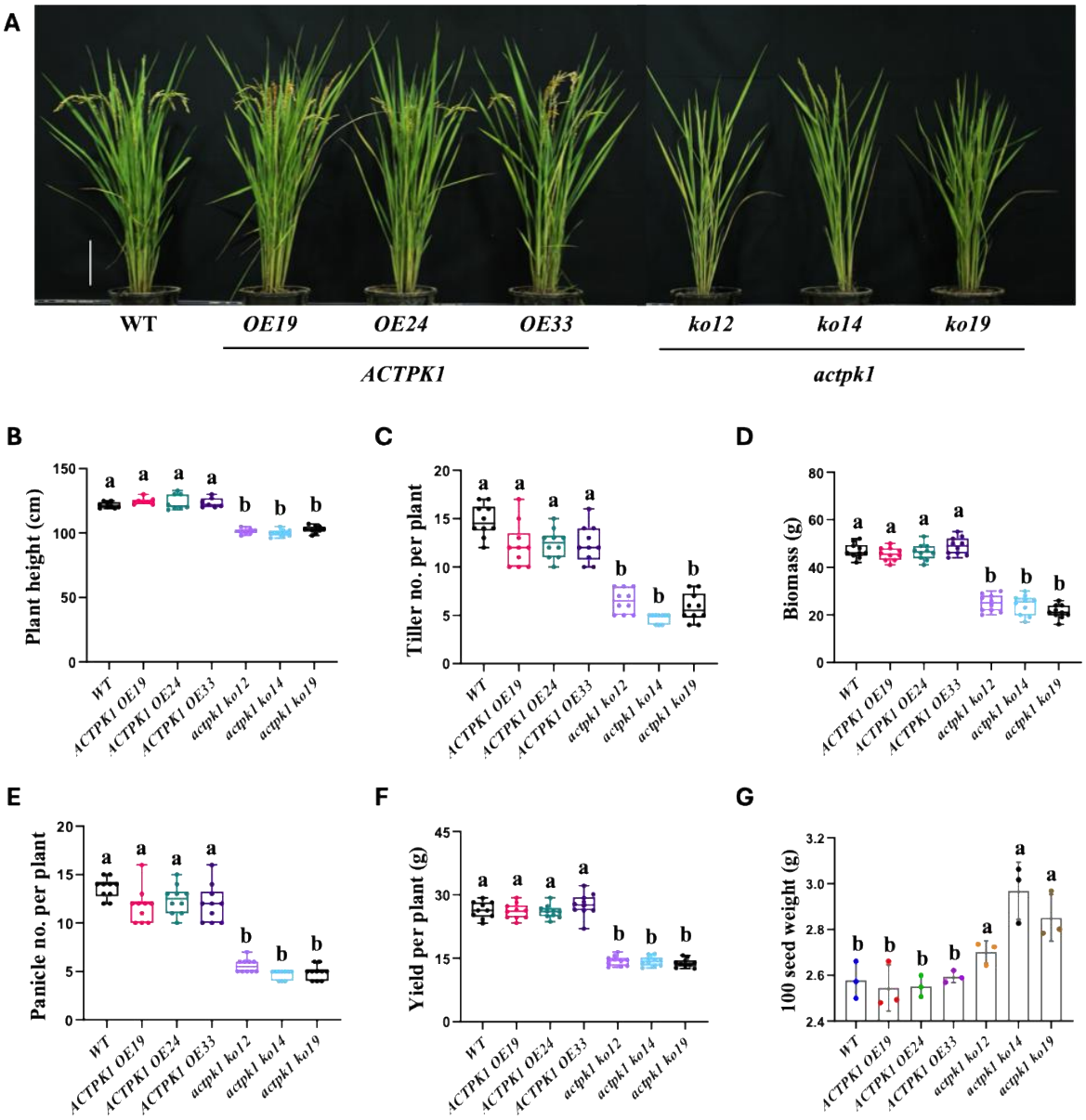

Fig. 7. ACTPK1 positively regulate plant biomass and yield. A) Representative image of WT, *ACTPK1 OE* (*ACTPK1 OE19, ACTPK1 OE24 & ACTPK1 OE33*) and *actpk1 ko* (*actpk1 ko12, actpk1 ko14 & actpk1 ko19*) plants. **B)-G)** Bar graph showing plant height **(B)**, tiller number per plant **(C)**, Biomass **(D)**, panicle number per plant **(E)**, yield per plant **(F)**, and 100 seed weight **(G)**, in WT, *ACTPK1 OE* (*ACTPK1 OE19, ACTPK1 OE24 & ACTPK1 OE33*) and *actpk1 ko* (*actpk1 ko12, actpk1 ko14 & actpk1 ko19*) plants. Values represent the mean ± SD (n = 10). Different letters indicate statistical significance according to one-way ANOVA followed by post-hoc Tukey HSD calculation at $P < 0.05$.

1319

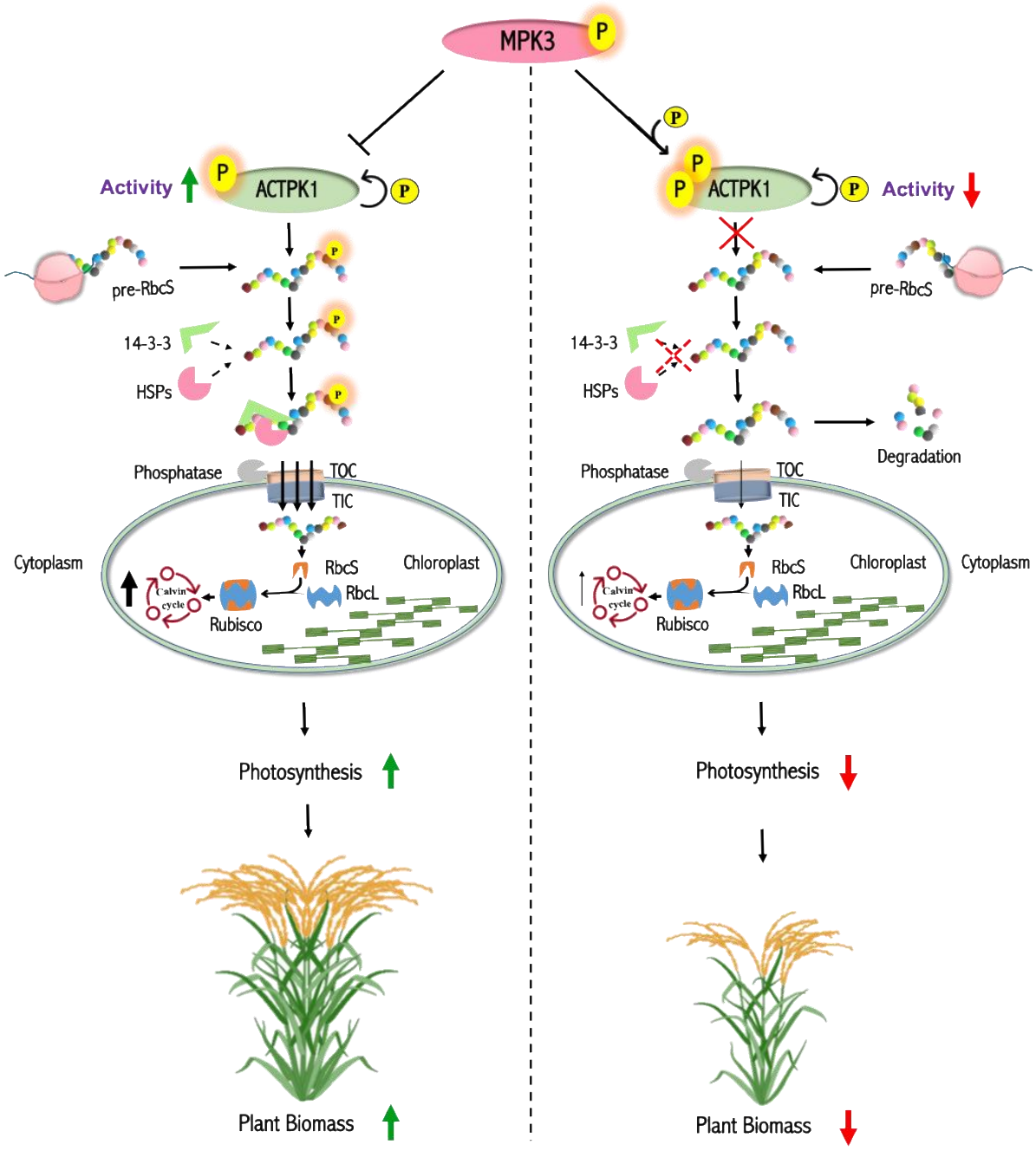

1320

1321 **Fig. 8. Diagrammatic representation depicting photosynthesis modulation by non-canonical MAPK**
1322 **cascade consisting of MPK3-ACTPK1-RbcS signalling module.** Activated MPK3 phosphorylates and
1323 suppresses ACTPK1 kinase activity. Active ACTPK1 in turn phosphorylates RbcS at Thr12, enhancing its
1324 cytosolic stability and promoting efficient chloroplast import. This non-canonical MAPK cascade
1325 governs Rubisco biogenesis, photosynthetic efficiency and thereby plant biomass.

1326

1327 **Supplemental Figures with legends:**

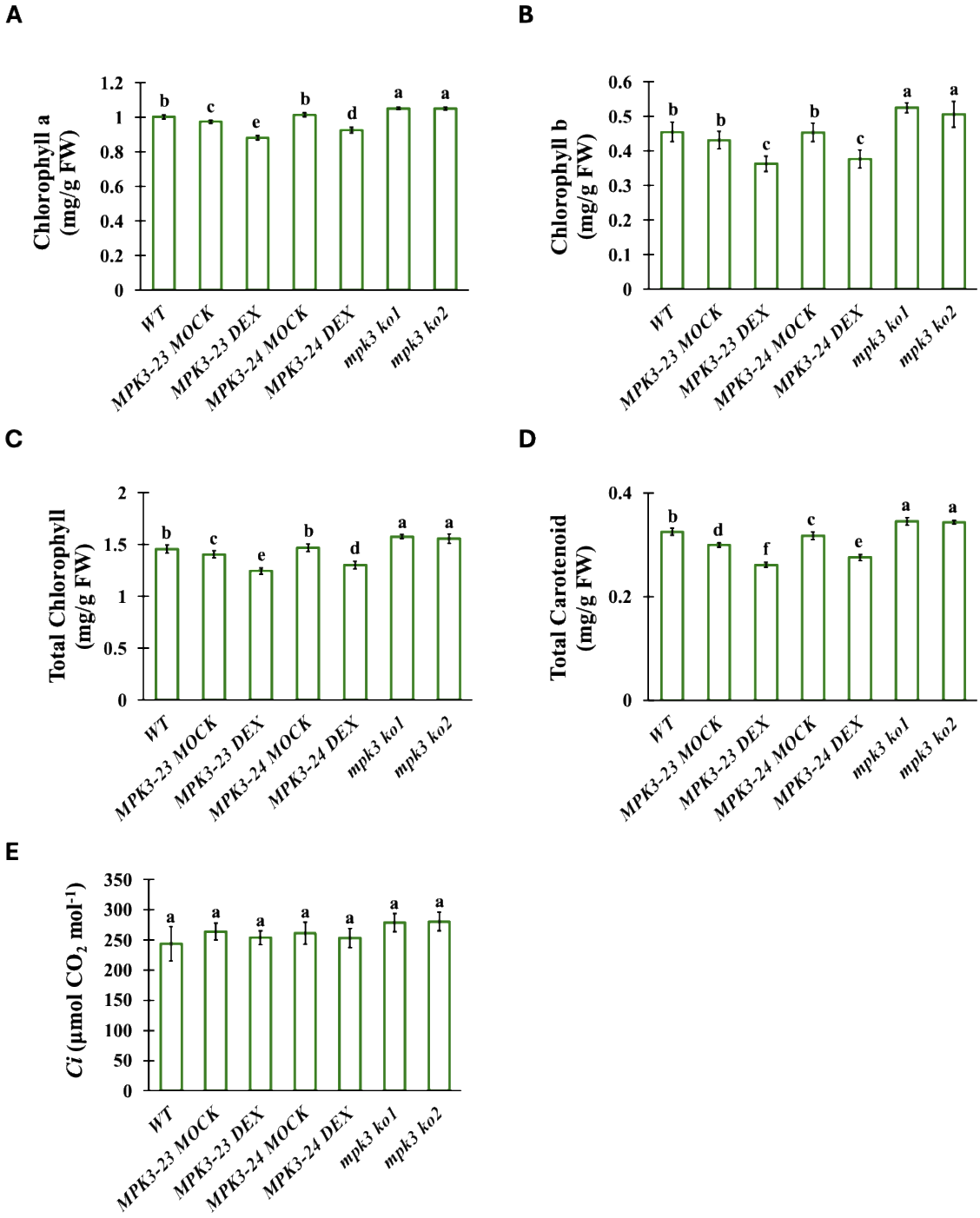

1328

1329 **Fig. S1. Photosynthetic pigments and parameters in WT, *MPK3 OE* (*MPK3-23*, *MPK3-24*)**
1330 **and *mpk3 ko* (*mpk3 ko1*, *mpk3 ko2*) lines. (A-D)** Bar graph showing the Chlorophyll a **(A)**,
1331 Chlorophyll b **(B)**, total chlorophyll **(C)**, and total carotenoid content **(D)** in WT, *MPK3 OE*
1332 (*MPK3-23*, *MPK3-24*) and *mpk3 ko* (*mpk3 ko1*, *mpk3 ko2*) lines. Each value represents mean
1333 ± SD, where n = 15 data points from different plants. Different letters indicate statistical
1334 significance according to one-way ANOVA followed by post-hoc Tukey HSD calculation at P
1335 < 0.05. **(E)** Bar graph representing intercellular CO_2 concentration at ambient CO_2 (400 µmol
1336 mol^{-1}) in WT, *MPK3 OE* (*MPK3-23*, *MPK3-24*) and *mpk3 ko* (*mpk3 ko1*, *mpk3 ko2*) lines. Each
1337 value represents mean ± SD, where n = 5 data points from different plants. Different letters
1338 indicate statistical significance according to one-way ANOVA followed by post-hoc Tukey HSD
1339 calculation at $P < 0.05$. MOCK, dimethyl sulfoxide treated (DMSO) plants; DEX,

1340 dexamethasone treated plants. 1 μM DMSO and DEX sprayed on *MPK3 OE* leaves, 24 h prior
1341 to taking measurements. All the photosynthetic measurements were taken from flag leaf at
1342 heading stage using LiCOR6800, between 8:00 am to 11:00 am.

1343

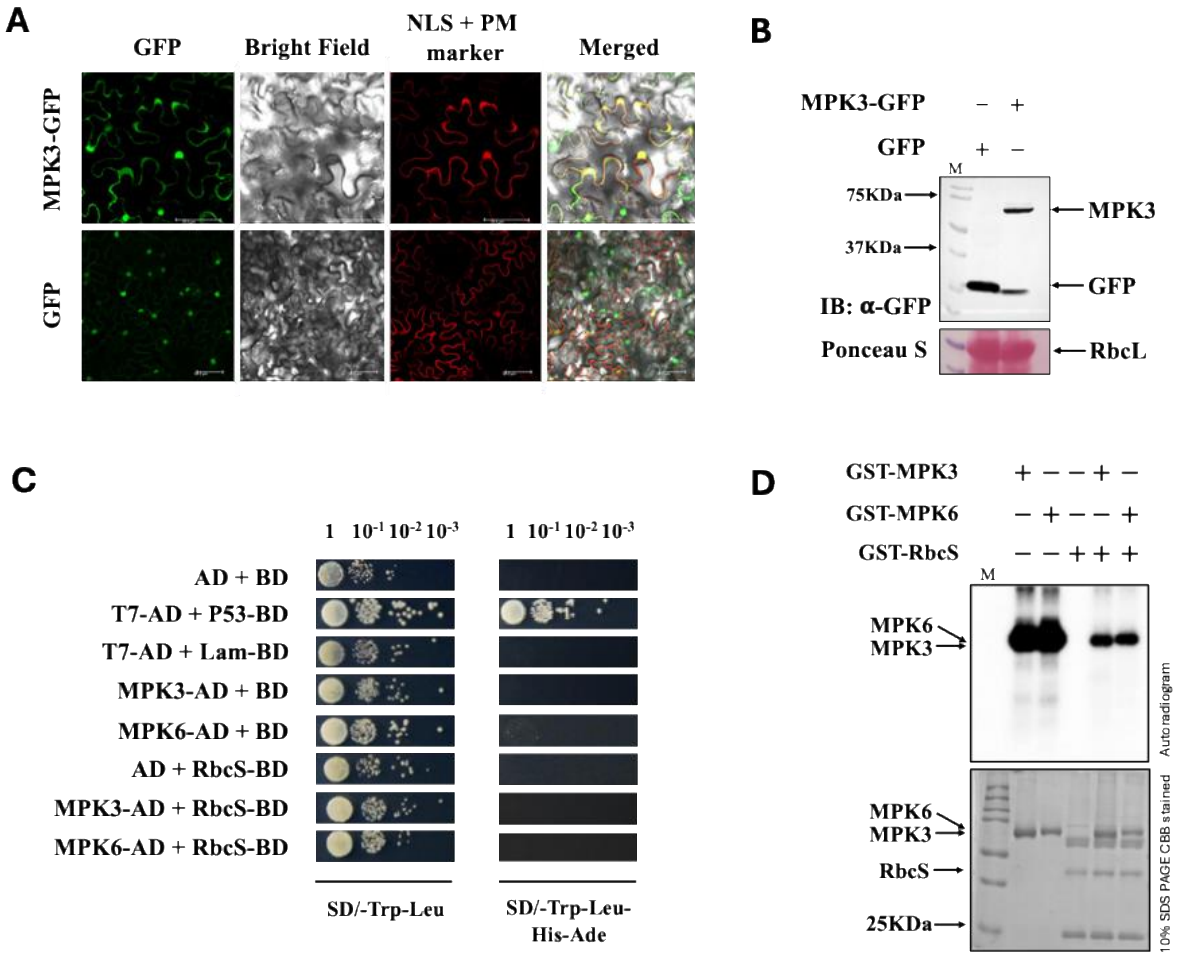

Fig. S2. Localisation of MPK3 and interaction and phosphorylation of RbcS with MPK3 and MPK6. (A) Confocal images depicting the localisation of MPK3 to nucleus and cytosol. Empty-GFP localisation served as negative control. Scale Bar, 25 *µ*m. **(B)** Western blots showing presence of MPK3 and GFP in confocal localisation samples of (A). Ponceau stained blot shows RbcL protein of *N. benthamiana*. **(C)** MPK3 and MPK6 does not interact with RbcS in yeast cells. Yeast cells were cultured on SD/-Trp-Leu and SD/-Trp-Leu-His-Ade media. AD, GAL4 activation domain; BD, GAL4 DNA-binding domain; SD, synthetic defined. **(D)** *In vitro* kinase assay showing GST-MPK3 and GST-MPK6 does not phosphorylate GST-RbcS. CBB stained 10% SDS PAA gel shows loaded proteins.

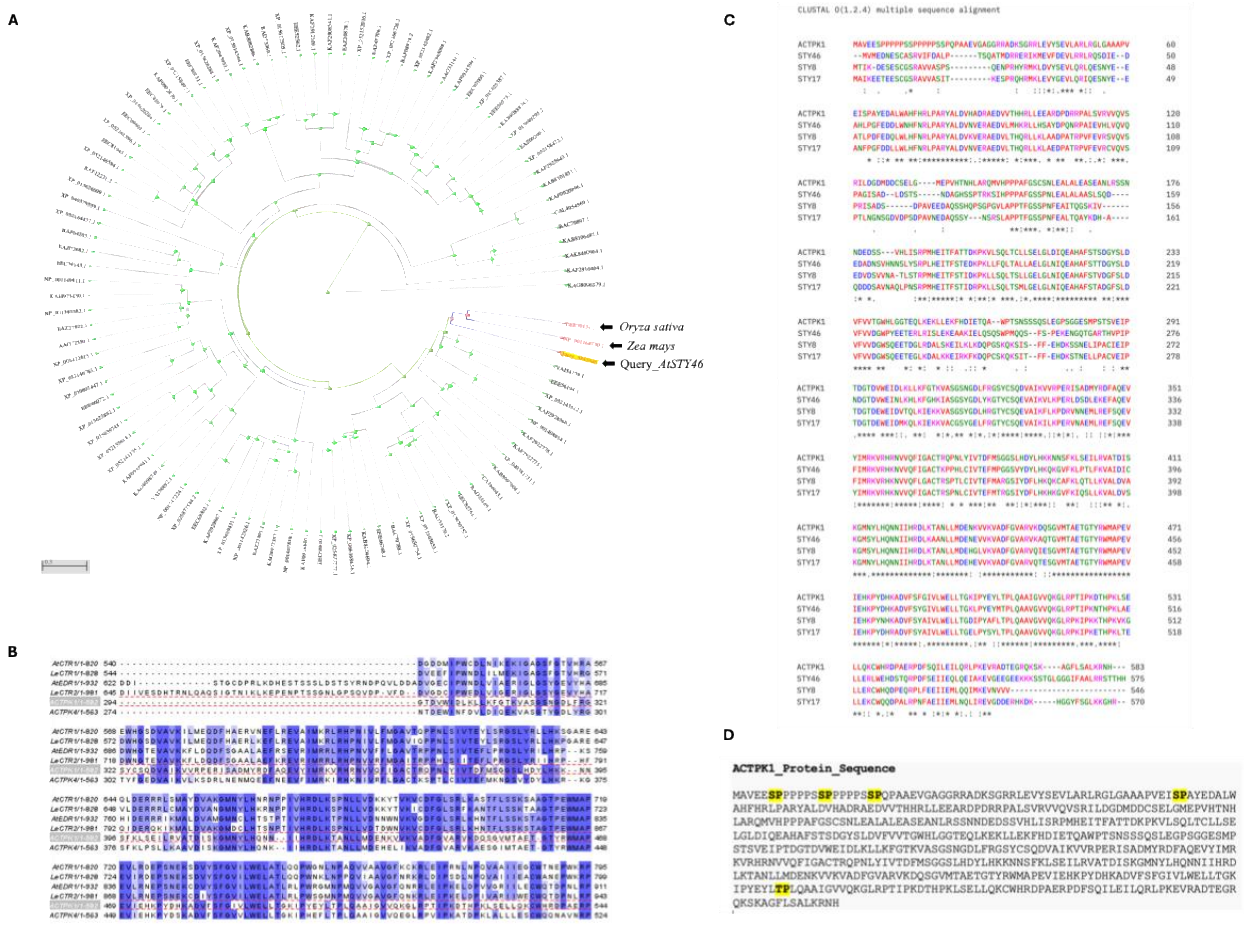

Fig. S3. ACTPK1 is a Raf-like MAPKKK exhibiting homology and sequence similarity with *At*STY8, *At*STY17 and *At*STY46, and contains multiple MAPK phosphorylation motifs. (A) Distant tree showing the homologues of *At*STY46. Accession numbers written in red are the closest homologue of *Arabidopsis* STY46 in *Zea mays* and *Oryza sativa*. Query sequence is taken as the AtSTY46 protein sequence against nr_cluster_seq database (NCBI) and the tree was produced by BLAST pairwise alignment. **(B)** Sequence Alignment of ACTPK1 Kinase domain with identified Plant Raf like MAPKKKs Kinase domain. Shaded boxes indicate identical residues. Prefixes on protein names indicate species of origin. *At*, *Arabidopsis thaliana*; *Le, Solanum lycopersicum var. lycopersicum.* Alignment was constructed using Clustal Ω program and analysed using Jalview software. **(C)** Sequence Alignment of ACTPK1 with AtSTY8, AtSTY17 and AtSTY46. Alignment was constructed using Clustal 0(1.2.4). **(D)** Protein sequence of ACTPK1 showing multiple MAPKs phosphorylation motifs (S/T followed by P). MAPKs phosphorylation motifs were highlighted in yellow colour.

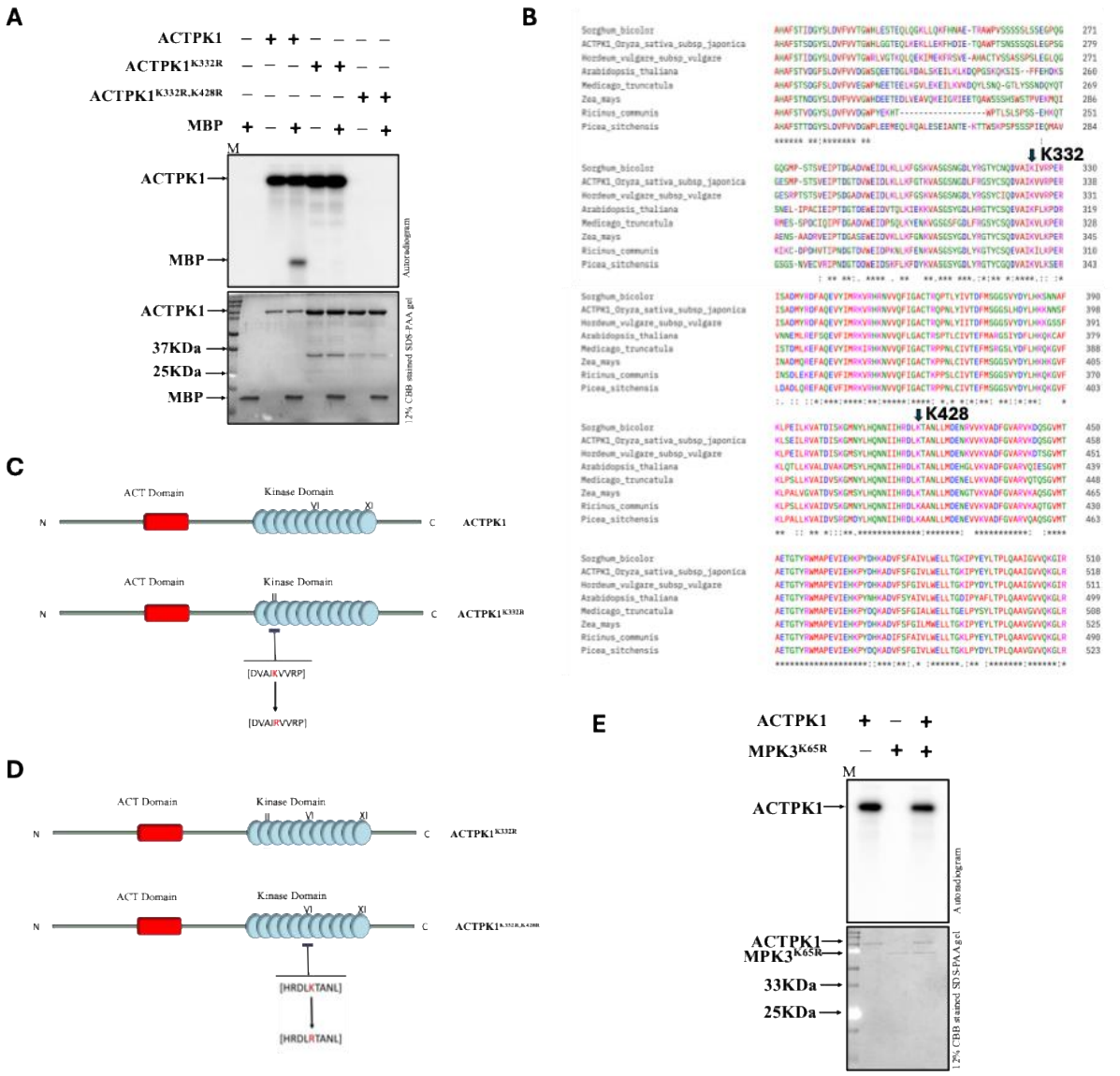

Fig. S4. Lysine at 332 and 428 are crucial for trans- and auto-phosphorylation activity of ACTPK1 and ACTPK1 do not phosphorylate MPK3. (A) *In vitro* phosphorylation assay depicting ACTPK1 showed auto- and trans-phosphorylation, ACTPK1^{K332R} showed only autophosphorylation and ACTPK1^{K332R,K428R} does not showed auto- or trans-phosphorylation. MBP was used as a substrate for ACTPK1, ACTPK1-GST, ACTPK1^{K332R}-GST, ACTPK1^{K332R,K428R}-GST. CBB stained 12% SDS PAA gel shows loaded proteins. **(B)** Diagrammatic representation showing the mutation created for generating ACTPK1^{K332R}. **(C)** Diagrammatic representation showing the mutation created for generating ACTPK1^{K332R,K428R}. **(D)** Sequence alignment of ACTPK1 kinase domain with its homologues from different plants showing the conservation of lysine at 332 (showed by black arrow followed by K332) and lysine at 428 (showed by black arrow followed by K428). Alignment was constructed using Clustal 0(1.2.4) **(E)** *In vitro* phosphorylation assay depicting ACTPK1 do not phosphorylates kinase dead MPK3^{K65R}-GST. CBB stained 12% SDS PAA gel shows loaded proteins.

1388

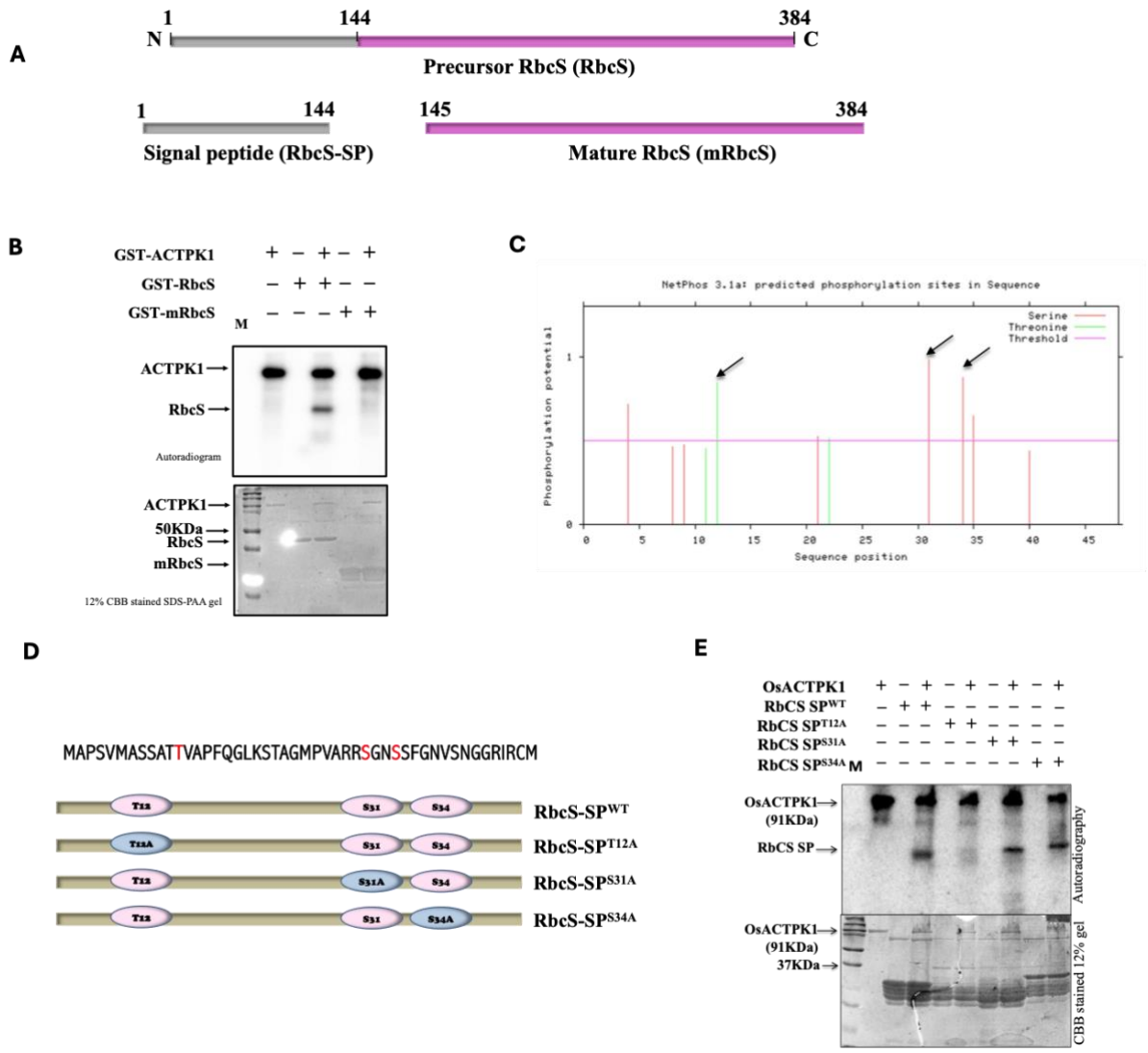

1389

1390 **Fig. S5. ACTPK1 phosphorylates RbcS at Thr12. (A)** Diagrammatic picture representing
1391 the truncation of precursor RbcS protein into signal peptide (RbcS-SP) and mature RbcS
1392 (mRbcS). **(B)** *In vitro* kinase assay showing ACTPK1 phosphorylates precursor RbcS (GST-
1393 RbcS) but not mature RbcS (mRbcS). CBB stained 12% SDS PAA gel shows loaded proteins.
1394 **(C)** NetPhos3.1 results showing the phosphorylation potential of different amino acids of RbcS.
1395 Black arrow indicates the amino acids having high phosphorylation potential score. **(D)**
1396 Pictorial representation of all the RbcS mutant constructs designed through site-directed
1397 mutagenesis. **(E)** *In vitro* kinase assay depicting Thr at 12 is the site of ACTPK1
1398 phosphorylation. CBB stained 12% SDS PAA gel shows loaded proteins.

1399

1400

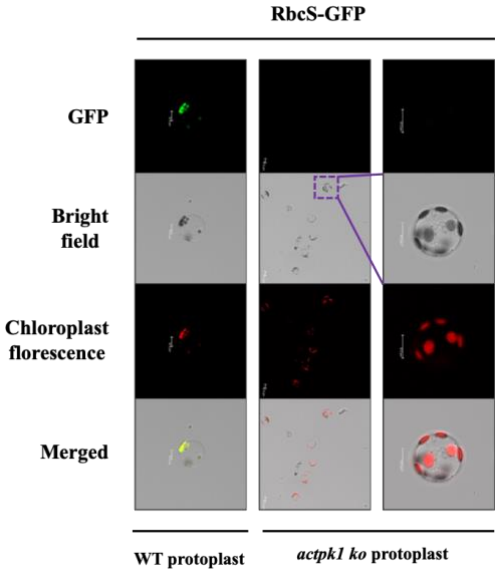

1401

1402 **Fig. S6. Absence of RbcS-GFP signal in *actpk1 ko* protoplasts.** Localization of RbcS in
1403 protoplast isolated from WT and *actpk1 ko* rice seedlings. Scale Bar, 10 μm. Third panel is
1404 the enlarged image of protoplast present in purple box of second panel.

1405

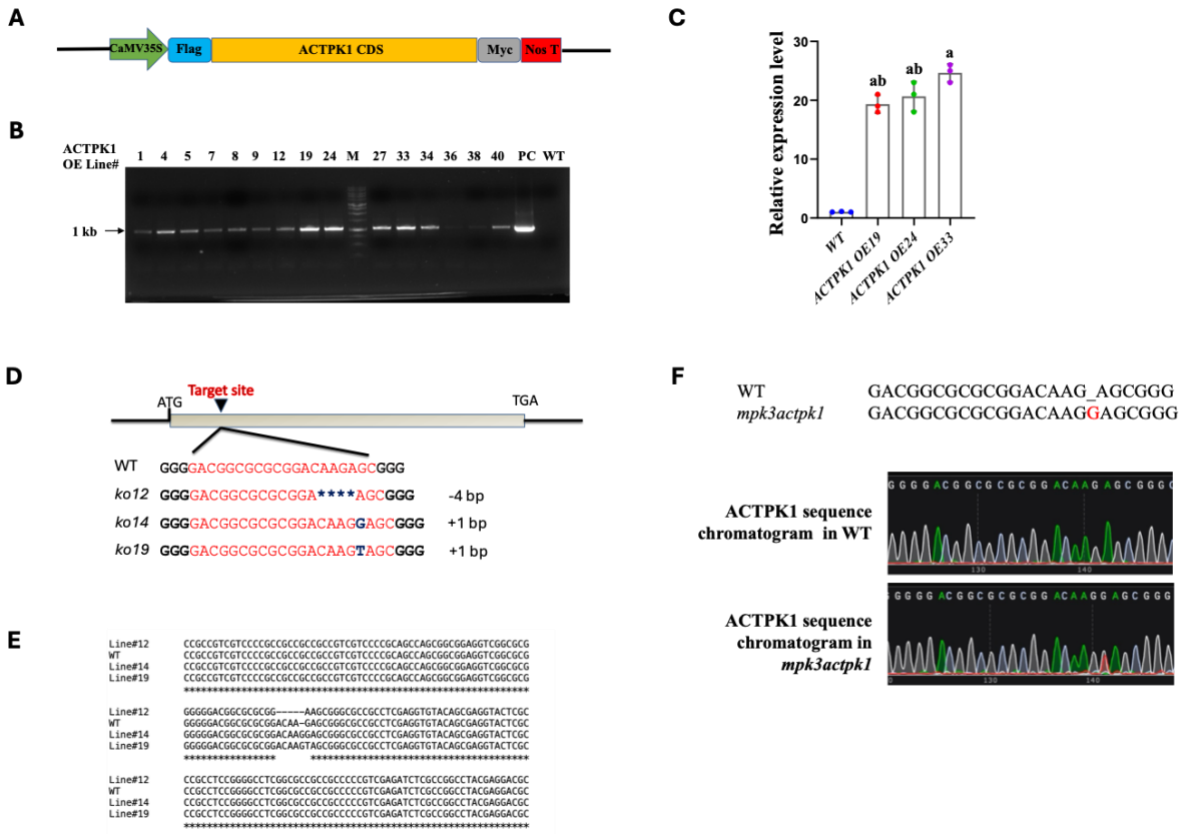

Fig. S7. Development of *ACTPK1 OE* and *actpk1 ko* lines. (A) Diagrammatic representation of the construct used for generating *ACTPK1 OE* plants **(B)** Nucleic acid gel image showing Semi-quantitative Real-time PCR analysis of *ACTPK1* expression in overexpression lines compared with WT plant. **(C)** Bar graph showing relative expression level of ACTPK1 in *ACTPK1 OE19, ACTPK1 OE24* and *ACTPK1 OE33* lines. Each value represents mean ± SD, where n = 3 biological replicates. Different letters indicate statistical significance according to one-way ANOVA followed by post-hoc Tukey HSD calculation at $P < 0.05$. **(D)** Diagrammatic representation of target site and sgRNA sequence and mutations observed in *actpk1 ko 12, actpk1 ko 14, and actpk1 ko 19* lines **(E)** Sequence alignment of different mutation identified from *actpk1 ko 12, actpk1 ko 14, and actpk1 ko 19* lines using clustal omega software. **(F)** Chromatogram of WT and *mpk3actpk1* showing insertion of G in coding region of ACTPK1 in *mpk3actpk1 ko* line. Inserted base is depicting in red colour. Knockout mutation in ACTPK1 was generated in the background of *mpk3 ko2.*

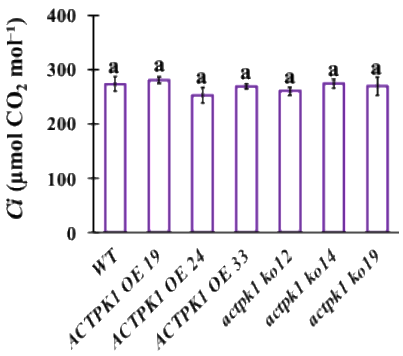

1421

1422 **Fig. S8. Intercellular CO_2 concentration in flag leaf of WT, *ACTPK1 OE* and *actpk1 ko***
1423 **plants.** Bar graph showing intercellular CO_2 concentration at ambient CO_2 (400 µmol mol^{-1}) in
1424 WT, *ACTPK1 OE* (ACTPK1 OE19, ACTPK1 OE24 and ACTPK1 OE33) and *actpk1 ko* (*actpk1*
1425 *ko 12, actpk1 ko 14, and actpk1 ko 19*) lines. Each value represents mean ± SD, where n = 5
1426 data points from different plants. Different letters indicate statistical significance according to
1427 one-way ANOVA followed by post-hoc Tukey HSD calculation at $P < 0.05$. All the
1428 photosynthetic measurements were taken from flag leaf at heading stage using LiCOR6800,
1429 between 8:00 am to 11:00 am.

1430

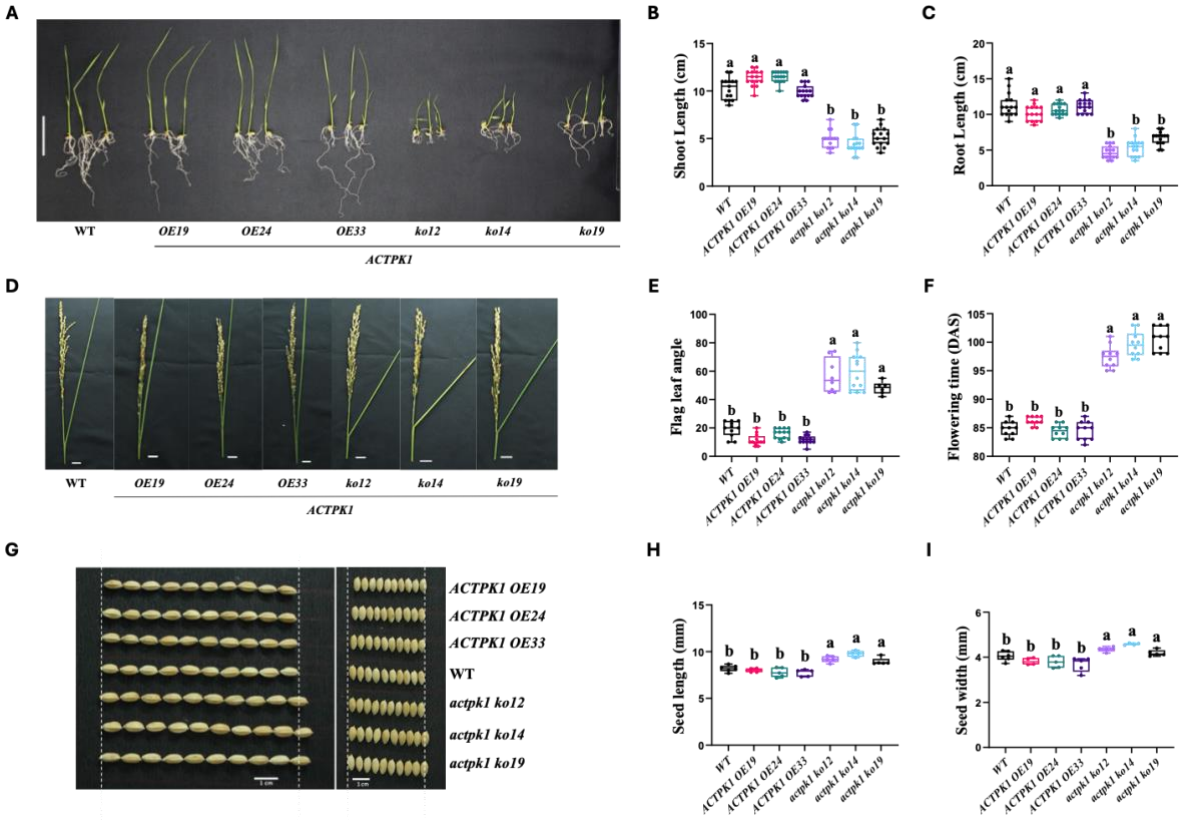

Fig. S9. ACTPK1 regulates vegetative growth, flag leaf angle, flowering time and seed architecture. (A) Representative images of WT, *ACTPK1 OE* and *actpk1 ko* seedlings. Scale Bar, 10 cm. **(B-C)** Bar graph showing shoot length (B) and root length (C) of 10 day old seedling of WT, *ACTPK1 OE* (ACTPK1 OE19, ACTPK1 OE24 and ACTPK1 OE33) and *actpk1 ko* (*actpk1 ko 12, actpk1 ko 14, and actpk1 ko 19*). Each value represents mean ± SD, where n = 10 data points. Different letters indicate statistical significance according to one-way ANOVA followed by post-hoc Tukey HSD calculation at $P < 0.05$. **(D)** Representative images depicting the flag leaf angle of WT, *ACTPK1 OE* and *actpk1 ko* plants**.** Scale Bar, 1 cm. **(E)** Bar graph depicting flag leaf angle of WT, *ACTPK1 OE* and *actpk1 ko* plants. Each value represents mean ± SD, where n = 10 data points. Different letters indicate statistical significance according to one-way ANOVA followed by post-hoc Tukey HSD calculation at $P < 0.05$. **(F)** Bar graph showing flowering time of WT, *ACTPK1 OE* and *actpk1 ko* plants. Each value represents mean ± SD, where n = 10 data points. Different letters indicate statistical significance according to one-way ANOVA followed by post-hoc Tukey HSD calculation at $P < 0.05$. **(G)** Representative pictures depicting the seed length and seed width of WT, (ACTPK1 OE19, ACTPK1 OE24 and ACTPK1 OE33) and *actpk1 ko* (*actpk1 ko 12, actpk1 ko 14, and actpk1 ko 19*) plants. Scale Bar, 1 cm. **(H-I)** Bar graph depicting the seed length (H) and seed width (I) of WT, *ACTPK1 OE* and *actpk1 ko* lines. Each value represents mean ± SD, where n = ~1000 data points from at least 5 different plants. Different letters indicate statistical significance according to one-way ANOVA followed by post-hoc Tukey HSD calculation at $P < 0.05$.

1455 **Supplemental Table 1**: Table containing the list of primers used in this study.

1456

Primer Name	Sequence (5`-3`)
Primers used for Gateway entry cloning	
MPK3 pENTR F	CACCATGGACGGGGCGCCGGTGGCGG
MPK3 pENTR R	GTACCGGAAGTTTGGGTTCATCTC
MPK6 pENTR F	CACCATGGACGCCGGGGCGCAGCCGTC
MPK6 pENTR R	CTGGTAATCAGGGTTGAACGCAAG
ACTPK1 pENTR F	CACCATGGCCGTGGAGGAGTCGCC
ACTPK1 pENTR R	GTGGTTTCTCTTCAATGCTG
RbcS pENTR F	CACCATGGCCCCCTCCGTGATG
RbcS pENTR R	GTTGCCACCAGACTCCTCGC
Primers used for Protein Expression	
MPK3 pGEX F	GGATCCATGGACGGGGCGCCGGTGGC
MPK3 pGEX R	CTCGAGCGGGTACCGGAAGTTTGGGT
MPK6 pGEX F	GGATCCATGGACGCCGGGGCGCAGCCG
MPK6 pGEX R	CTCGAGCTGGTAATCAGGGTTGAAC
ACTPK1 pGEX F	CACCGAATTCCCATGGCCGTGGAGGAGTCGC
ACTPK1 pGEX R	CCGTCGACGTGGTTTCTCTTCAATGC
RbcS pGEX F	TTGGATCCATGGCCCCCTCCGTGATG
RbcS pGEX R	TTGTCGACGCCACCAGACTCCTCGCA
RbcS-SP pGEX F	TTGGATCCATGGCCCCCTCCGTGATG
RbcS-SP pGEX R	TTGTCGACCCTGATCCTGCCGCCATTGC
mRbcS pGEX F	CACCCAGGTGTGGCCGATTGAGGGCAT
mRbcS pGEX R	TTGTCGACGCCACCAGACTCCTCGCA
Primers used for Yeast-2 Hybrid assay	
ACTPK1 AD/BD F	AAGAATTCATGGCCGTGGAGGAGT
ACTPK1 AD/BD R	CCGGATCCGTGGTTTCTCTTCAATGC
MPK3 AD/BD F	CATATGATGGACGGGGCGCCGGT
MPK3 AD/BD R	GGATCCGTACCGGAAGTTTGGGT
MPK6 AD/BD F	GGATCCGGATGGACGCCGGGGCGCAGC
MPK6 AD/BD F	GGATCCGCTACTGGTAATCAGGGTTG
Primers used for developing and screening transgenic plants	

Cas9 F	AACAGCCGCGAGAGAATGAA
Cas9 R	TCGGCCTTGGTCAGATTGTC
ACTPK1 sgRNA F	GGCAGACGGCGCGCGGACAAGAGC
ACTPK1 sgRNA R	AAACGCTCTTGTCCGCGCGCCGTC
ACTPK1 Crispr_Seq F	TCTCCTCTCTCGTCTCGTG
ACTPK1 Crispr_Seq R	CATGGATGGATCTCTCTCA
CaMV 35S_F	CCACCATGTTGGCATGGAGTCAAAGATTCAAAT AG AG
CaMV 35S_R	GAATTCAGTCCCCCGTGTTCTCTCCAAATG
FLAG_F	GGATCCATGGACTATAAGGACCACGAC
SDM	
ACTPK1 K332R F	AGTCAGGATGTAGCTATTAGAGTAGTGAGACCT GAACGC
ACTPK1 K332R R	GCGTTCAGGTCTCACTACTCTAATAGCTACATC CTGACT
ACTPK1 K428R F	CATAATTCACCGTGATCTCAGGACAGCGAATCT TCTTATGG
ACTPK1 K428R F	CCATAAGAAGATTCGCTGTCCTGAGATCACGGT GAATTATG
MPK3 K65R F	GATGGTGGCGATACGCAAGATCGCCAACGC
MPK3 K65R R	GCGTTGGCGATCTTGCGTATCGCCACCATC
RbcS T12A F	CACCATGGCCCCCTCCGTGATGGCGTCGTCGG CCACCGCCGTCGCTCCCTTC
RbcS T12A R	GTTGCCACCAGACTCCTCGC
RbcS S31A F	CACCATGGCCCCCTCCGTGATG
RbcS S31A R	CATGCACCTGATCCTGCCGCCATTGCTGACGTT GCCGAAGCTGGCGTTGCCGGAGCGGC
RbcS S34A F	CACCATGGCCCCCTCCGTGATG
RbcS S34A R	CATGCACCTGATCCTGCCGCCATTGCTGACGTT GCCGAAGCTGGAGTTGCCGGCGCGGC
RbcS T12D F	CACCATGGCCCCCTCCGTGATGGCGTCGTCGG CCACCGACGTCGCTCCCTTC
RbcS T12D R	GTTGCCACCAGACTCCTCGC

1457